Chapter 8

# Self-Consistent Homogenization Methods for Predicting Forming Limits of Sheet Metal

Javier W. Signorelli and María de los Angeles Bertinetti

Additional information is available at the end of the chapter

http://dx.doi.org/10.5772/50662

## 1. Introduction

Formability of sheet metals can be characterized by the forming-limit diagram (FLD). This concept has proved to be extremely useful for representing conditions leading to the onset of sheet necking (Hecker, 1975), and now is one of the best tools available to metallurgical engineers to assess a particular steel sheet's ability to be drawn or stretched. In a single diagram, the FLD represents all combinations of critical-limit surface strains corresponding to failure. Within the FLD, a line called forming-limit curve (FLC) separates the region of uniform sheet deformation from the region of slightly greater deformation, where the sheet will likely develop a local deformation instability or neck. Experimental measurement of the FLD is not an easy task, requiring a wide range of sample geometries and even more than one type of mechanical test. Also, many test factors measurably affect the limit-strain determination: friction conditions, small deviations in loading paths due bending effects, and strain-measurement procedures. Similarly, several physical factors related to material properties (e.g. plastic anisotropy, work hardening and strain-rate sensitivity) have an important influence in the development of localized necking or failure. Numerical simulation promotes a better understanding of deformation and failure in polycrystal sheet metal aggregates, by examining issues related to crystal anisotropy and stress / strain heterogeneity.

Considerable effort has recently been made to develop theoretical models for predicting the FLD behavior. Most of them are based either on a bifurcation analysis (Storen & Rice, 1975) or a model where the strain instability appears in the deformation process due to an imperfection already present in the material (Marciniak & Kuczynski, 1967). The latter, MK from now on, has probably been the most widely used of the two techniques. Within the MK framework, the influence of various constitutive features on FLDs has been explored using phenomenological plasticity models and crystal plasticity. In recent years, research has shown that the localization of plastic flow is influenced by deformation anisotropy (Asaro & Needleman, 1985; Tóth et al., 1996; Wu et al., 2004a; Lee & Wen, 2006). Thus,

crystal-plasticity models should provide a framework for better understanding the relation between flow localization and material microstructure. Issues such as yield-surface shape – changes of sharpness – material anisotropy – crystal reorientation – are directly addressed within a polycrystalline model. It is widely recognized that the crystallographic texture strongly affects forming-limit diagrams and the macroscopic anisotropy of polycrystalline sheet metals. Numerous authors have adopted the MK model in conjunction with a crystal plasticity model to describe strain localization in rolled sheets (Kuroda & Tvergaard, 2000; Knockaert et al., 2002; Wu et al., 2004a; Inal et al., 2005; Yoshida et al., 2007; Neil & Agnew, 2009). Based on this strategy, the authors have examined how plastic anisotropy influences limit strains (Signorelli et al., 2009). For the FLD simulations, crystallographic effects were taken into account by combining the MK approach with a viscoplastic (VP) self-consistent (SC) and a Full-Constraint (FC) crystal-plasticity model, MK-VPSC and MK-FC respectively.

In this chapter we will analyze the influence that the numerous microstructural factors characterizing metals have on forming-limit strains. Moreover, we will focus on the consequences that selecting either a FC or SC type grain-interaction model has on numerical results. We will start, in the following section, with a brief description of the texture and anisotropy of cubic metals. The representation of crystallographic texture and the determination of the polycrystal texture are addressed. The material´s plastic deformation as a result of crystallographic dislocation motion on the active slip systems is discussed at the end of the section. The single crystal properties and the way in which grains interact in a polycrystal are the subject of Section 3. An outline of the implementation of the VPSC formulation in conjunction with the well-known MK approach for modeling localized necking closes the section. A parametric analysis of the influence of the initial-imperfection intensity and orientation, strain-rate sensitivity and hardening on the limit strains is the content of Section 4. In Section 5 the MK-FC and MK-VPSC approaches will be examined in detail. FLDs will be predicted for different materials in order to clearly illustrate the differences between the FC or the VPSC homogenization schemes, particularly in biaxial stretching.

## 2. Texture and anisotropy of cubic metals

Plastic anisotropy of polycrystals arises from crystallographic texture. In a material with a plasticity-induced texture, anisotropy at the microscopic level is determined by the different ways in which the material is deformed. In metals, plastic deformation occurs by crystallographic slip, due to the movement of dislocations within the lattice. In general, slip takes place on the planes which possess the highest atomic density, *slip planes*, and in the most densely packed directions, *slip directions*. The slip plane is characterized by the unit vector **n**, which is normal to the plane, and the slip direction, represented by the unit vector **b** (Burger's vector). The combination of both vectors, which are perpendicular to each other, defines a *slip system*.

Since crystallographic slip is limited to certain planes and directions, the applied stress required to initiate plastic flow depends on the orientation of the stress relative to the crystallographic axis of the crystal. If the plane is either normal or parallel to the applied stress, the shear stress on the plane is zero and no plastic deformation is possible. Slip begins

when the shear stress on a slip system reaches a critical value $\tau_c$. This yield criterion is called *Schmid´s Law*. In most crystals slip can occur either in the **b** or **–b** direction.

Figure 1 shows a slip system represented by the vectors **n** and **b.** Suppose that the crystal has a general state of stress $\sigma_{ij}$ acting on it referenced to the coordinate system **S** (**S** is fixed to the sample). The shear stress $\sigma'_{12}$ acting on the slip system can be obtained by transforming the stress tensor $\sigma_{ij}$ from the **S** to the **S′** system (**S′** is fixed to the slip system). Using the typical equations for tensor transformation, the resolved shear stress acting on the slip system is:

$$\tau_r = \sigma'_{12} = b_i \; n_j \; \sigma_{ij} \tag{1}$$

If the crystal is loaded in tension along the $X_3$ axis, the shear stress acting on the slip plane is

$$\tau_r = \sigma \cos\lambda \cos\phi, \tag{2}$$

where $\lambda$ is the angle between the slip direction and the tensile axis, and $\phi$ is the angle between the tensile axis and the normal to the slip plane.

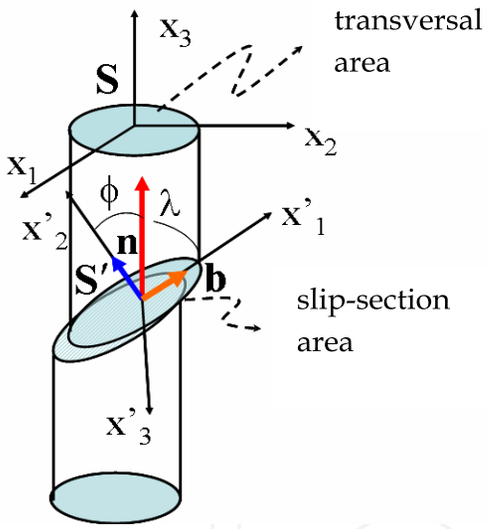


**Figure 1.** A schematic diagram of slip in the direction **b** occurring on a plane with the normal **n**.

In FCC materials, the crystallography of slip is simple, it takes place on the most densely packed planes {111} and in the most densely packed directions <110>. In BCC metals, the most common mode of deformation is {110}<111>, but these materials also slip on other planes: {112} and {123} with the same slip direction. Plastic deformation occurs by 12 crystallographic slip systems of the type {111}<110> for FCC metals and 48 slip systems of the type {110}<111>, {112}<111> and {123}<111> for the BCCs (see Table 1). A slip line is the result of a displacement of the material along a single lattice plane through a distance of about a thousand atomic diameters. The slip lines are visible traces of slip planes on the surface, and they can be observed when a metal with a polished surface is deformed plastically. As an example, in the optical micrograph shown in Figure 2, the slip bands appear as long steps on the surface. The terraced appearance is produced when the slip planes meet the crystal surface.

| Metals | Slip systems | | | | | |
|---|---|---|---|---|---|---|
| FCC (Cu, Ni, Al, Pb Au, γFe) | <110>{111} | | | | | |
| 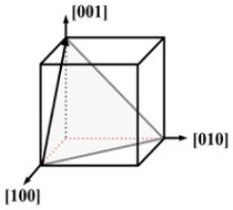 | 0 | 1 | 1 | 1 | 1 | -1 |
| | 1 | 0 | 1 | 1 | 1 | -1 |
| | 1 | -1 | 0 | 1 | 1 | -1 |
| | 0 | 1 | -1 | 1 | -1 | -1 |
| | 1 | 0 | 1 | 1 | -1 | -1 |
| | 1 | 1 | 0 | 1 | -1 | -1 |
| | 0 | 1 | 1 | 1 | -1 | 1 |
| | 1 | 0 | -1 | 1 | -1 | 1 |
| | 1 | 1 | 0 | 1 | -1 | 1 |
| | 0 | 1 | -1 | 1 | 1 | 1 |
| | 1 | 0 | -1 | 1 | 1 | 1 |
| | 1 | -1 | 0 | 1 | 1 | 1 |



Figure 2: Slip lines on the surface of a Cu polycrystal.

| Metals | Slip systems | | | | | |
|---|---|---|---|---|---|---|
| BCC (αFe, Nb, W, Cr, V, Mo) | {110}<111> | | | | | |
| 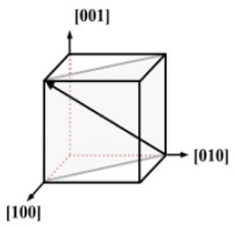 | 0 | 1 | 1 | 1 | 1 | -1 |
| | 1 | 0 | 1 | 1 | 1 | -1 |
| | 1 | -1 | 0 | 1 | 1 | -1 |
| | 0 | 1 | -1 | 1 | -1 | -1 |
| | 1 | 0 | 1 | 1 | -1 | -1 |
| | 1 | 1 | 0 | 1 | -1 | -1 |
| | 0 | 1 | 1 | 1 | -1 | 1 |
| | 1 | 0 | -1 | 1 | -1 | 1 |
| | 1 | 1 | 0 | 1 | -1 | 1 |
| | 0 | 1 | -1 | 1 | 1 | 1 |
| | 1 | 0 | -1 | 1 | 1 | 1 |
| | 1 | -1 | 0 | 1 | 1 | 1 |
| | {112}<111> | | | | | |
| 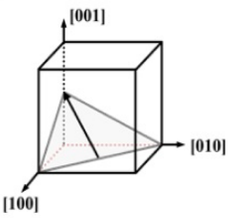 | -2 | 1 | 1 | 1 | 1 | 1 |
| | 1 | -2 | 1 | 1 | 1 | 1 |
| | 1 | 1 | -2 | 1 | 1 | 1 |
| | 2 | 1 | 1 | -1 | 1 | 1 |
| | -1 | -2 | 1 | -1 | 1 | 1 |
| | -1 | 1 | -2 | -1 | 1 | 1 |
| | -2 | -1 | 1 | 1 | -1 | 1 |
| | 1 | 2 | 1 | 1 | -1 | 1 |
| | 1 | -1 | -2 | 1 | -1 | 1 |
| | 2 | -1 | 1 | -1 | -1 | 1 |
| | -1 | 2 | 1 | -1 | -1 | 1 |
| | -1 | -1 | -2 | -1 | -1 | 1 |
| | {123}<111> | | | | | |
| 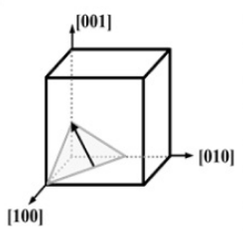 | 3 | -1 | -2 | 1 | 1 | 1 |
| | 3 | -2 | -1 | 1 | 1 | 1 |
| | -1 | 3 | -2 | 1 | 1 | 1 |
| | -2 | 3 | -1 | 1 | 1 | 1 |
| | -1 | -2 | 3 | 1 | 1 | 1 |
| | -2 | -1 | 3 | 1 | 1 | 1 |
| | 3 | 1 | 2 | -1 | 1 | 1 |
| | 3 | 2 | 1 | -1 | 1 | 1 |
| | 1 | 3 | -2 | -1 | 1 | 1 |
| | 2 | 3 | -1 | -1 | 1 | 1 |
| | 1 | -2 | 3 | -1 | 1 | 1 |
| | 2 | -1 | 3 | -1 | 1 | 1 |
| | 3 | 1 | -2 | 1 | -1 | 1 |
| | 3 | 2 | -1 | 1 | -1 | 1 |
| | 1 | 3 | 2 | 1 | -1 | 1 |
| | 2 | 3 | 1 | 1 | -1 | 1 |
| | -1 | 2 | 3 | 1 | -1 | 1 |
| | -2 | 1 | 3 | 1 | -1 | 1 |
| | 3 | -1 | 2 | -1 | -1 | 1 |
| | 3 | -2 | 1 | -1 | -1 | 1 |
| | -1 | 3 | 2 | -1 | -1 | 1 |
| | -2 | 3 | 1 | -1 | -1 | 1 |
| | 1 | 2 | 3 | -1 | -1 | 1 |
| | 2 | 1 | 3 | -1 | -1 | 1 |



**Table 1.** Slip systems of FCC and BCC cubic metals.

## 2.1. Crystal orientation

A polycrystal is composed of crystals, each with a particular crystallographic orientation. Several parameters are involved in characterizing a polycrystal, such as the shape, size, crystallographic orientation and position of each grain inside the sample. The orientation of each crystal in the polycrystal can be defined by a rotation from the sample coordinate system to the crystal coordinate system. The sample coordinate system is referenced to the sample, and it can be chosen arbitrarily. For an example, the *Rolling Direction* (RD), the *Transverse Direction* (TD) and the *Normal Direction* (ND) are typically chosen as sample coordinate system for a rolled sheet. The orientation relation between a single crystal and the sample coordinate systems may be thought of as rotating one frame into the other. Euler angles are useful for describing one frame in term of the other, or vice versa. Several different notations have been used to define these angles, but that of Bunge is most common and will be used in this chapter (Bunge, 1982). These three angles represent three consecutive rotations that must be given to each grain to bring its crystallographic <100> axes into coincidence with the sample axes. This is equivalent to saying that any orientation can be obtained by conducting three elemental rotations (rotations around a single axis). Consequently, any rotation matrix can be decomposed into a product of three elemental rotation matrices. The matrix rotation (Eq. 3), written in terms of Euler angles $(\varphi_1, \phi, \varphi_2)$, is obtained by multiplication of the elementary matrices defining the three successive Euler rotations: i) a rotation about the Z-axis through the angle $\varphi_1$, ii) a rotation about the new X-axis through the angle $\phi$ and iii) a rotation about the last Z-axis through an angle $\varphi_2$. This gives the crystal coordinate system (see Figure 3).

$$\begin{pmatrix} \cos\varphi_1\cos\varphi_2 - \sin\varphi_1\sin\varphi_2\cos\phi & \sin\varphi_1\cos\varphi_2 + \cos\varphi_1\sin\varphi_2\cos\phi & \sin\varphi_2\sin\phi \\ -\cos\varphi_1\sin\varphi_2 - \sin\varphi_1\cos\varphi_2\cos\phi & -\sin\varphi_1\sin\varphi_2 + \cos\varphi_1\cos\varphi_2\cos\phi & \cos\varphi_2\sin\phi \\ \sin\varphi_1\sin\phi & -\cos\varphi_1\sin\phi & \cos\phi \end{pmatrix} \quad (3)$$

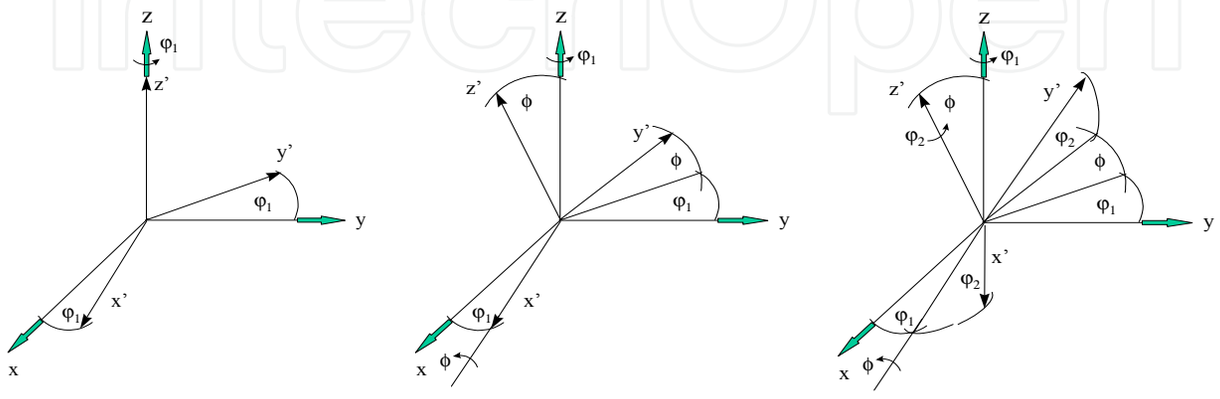


**Figure 3.** Definition and sequence of rotation through the different Euler angles.

## 2.2. Crystallographic texture

Texture refers to a non-uniform distribution of crystallographic orientations in a polycrystal. The textures of rolled or rolled and recrystallized sheets have been most widely investigated in metallurgy. Crystallographic orientations in rolled sheets are generally represented as being of the type {hkl}<uvw>, where {hkl} are the grain planes that lie parallel to the plane of the sheet. On the other hand, the <uvw> directions lie parallel to the rolling direction. Conventionally, the standard method of representing textures was by means of pole figures. However, while pole figures provide a useful description of texture, the information they contain is incomplete. A complete description can be obtained by the Orientation Distribution Function (ODF), which describes the orientation of all individual grains in the aggregate.

### *2.2.1. Pole figures*

Texture measurements are used to determine the orientation distribution of crystalline grains in a polycrystalline sample. There are several experimental methods that can be used to measure texture. The most popular is X-ray diffraction. A pole figure – which is a projection that shows how the specified crystallographic directions of grains are distributed in the sample reference frame – results from an X-ray diffraction texture measurement. This representation must contain some reference directions that relate to the material itself. Generally these directions refer to the forming process.

The inverse pole figure is a particularly useful way to describe textures produced from deformation processes. In this case only a single axis needs to be specified. An inverse pole figure shows how the selected direction in the sample reference frame is distributed in the reference frame of the crystal. The frequency with which a particular crystallographic direction coincides with the sample axis is plotted in a single triangle of the stereographic projection.

### *2.2.2. ODF and Euler space*

The ODF specifies the probability density for the occurrence of particular orientations in the Euler space. This space is defined by the three Euler angles, which are required to fully describe a single orientation. Mathematical methods have been developed that allow an ODF to be calculated from the numerical data obtained from several pole figures. The most widely adopted notations employed for these description were those proposed independently by Bunge and Roe. They used generalized spherical harmonic functions to represent crystallite distributions (A detailed description of the mathematics involved can be found in Bunge, 1982). ODF analysis was developed originally for materials with cubic crystallography and orthorhombic sample symmetry, i.e. for sheet products. In the Bunge notation, for cubic/orthotropic crystal/sample symmetry, a three dimensional orientation volume may be defined by using three orthogonal axes for $\varphi_1$, $\phi$ and $\varphi_2$, with each ranging from 0º to 90º. The value of the orientation density at each point in Euler space is the strength or intensity of that orientation in multiples of random units.

Most of the texture data available in the literature and almost all of the ODF data refer to rolled materials. The information contained in a three-dimensional ODF can be expressed in terms of typical components and fibers for cubic symmetry materials. A fiber is a range of orientations limited to a single degree of freedom about a fixed axis, which appears as a line that may or may not lie entirely in one section of ODF. The ideal components and fibers are associated with more or less constant intensity for a group of orientations related to one another by rotations around a particular crystallographic direction.

During cold rolling of FCC metals, two crystallographic fibers arise: the α-fiber containing <110>//ND orientations and extending from *Goss* {110}<001> to *Brass* {110}<112>; and the β-fiber which starts at *Brass*, runs through *S* {123}<634>, and finally reaches C*opper* {112}<111>. The β-fiber contains the most stable components of the rolling texture (Humphreys & Hatherly, 2004). Considering recrystallized rather than rolled material, the typical texture components are C*ub*e {001}<100> and *Goss*. Table 2 shows a schematic representation of the rolling texture characteristic of the {111} pole figure (left) and the main texture components for FCC (right). The nature of the FCC rolling texture is such that the data are best displayed in $\varphi_2$ sections, while the typical {100} and {111} pole figures best represent these orientations.

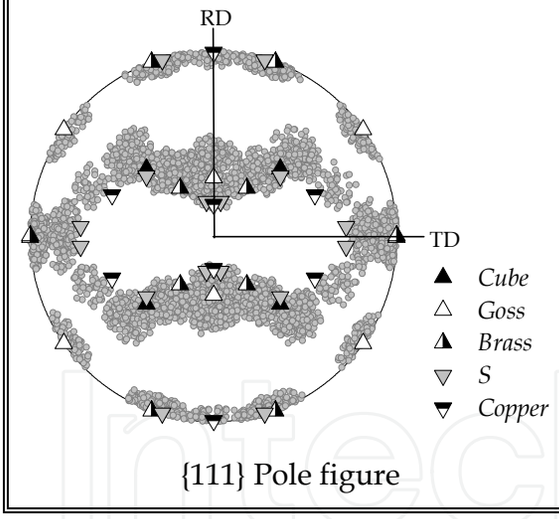


| Typical texture components in rolled FCC metals | | | | | |
|---|---|---|---|---|---|
| Component | {hkl} | <uvw> | $\varphi_1$ | $\phi$ | $\varphi_2$ |
| *Copper* | 112 | 111 | 90º | 35º | 45º |
| *S* | 123 | 634 | 59º | 37º | 63º |
| *Goss* | 011 | 100 | 0º | 45º | 0/90º |
| *Brass* | 011 | 211 | 35º | 45º | 0/90º |
| *Cube* | 001 | 100 | 0º | 0º | 0º |

**Table 2.** FCC rolling components.

Cold rolling and recrystallization textures in BCC metals are commonly described in terms of five ideal orientations: {001}<110>, {112}<110>, {111}<110>, {111}<112> and {554}<225>. The positions of theses orientations in the {100} pole figure are shown at the left in Table 3. In general, BCC metals and alloys tend to form fiber textures. That is most orientations are assembled along two characteristic fibers that run through orientation space: the α-fiber and the γ-fiber. The RD or α-fiber runs from {001}<110> to {111}<110>, containing orientations with the <110> axis parallel to RD, and the γ-fiber runs from {111}<110> to {111}<112>, gathering orientations with a <111> axis parallel to ND. The two fibers intersect at the

{111}<110> component (Ray et al., 1994). The data are best displayed by sections at constant values of $\varphi_1$, but the most important texture features can all be found in the $\varphi_2 = 45^{\circ}$ section (right in Table 3). Table 3 also gives the Miller indices and Euler angles of the typical BCC texture components. The {100} and {110} pole figures best represent the ideal BCC material orientations.

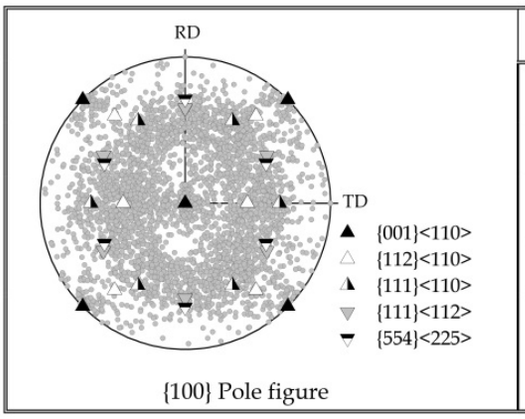


Typical texture components in rolled BCC metals

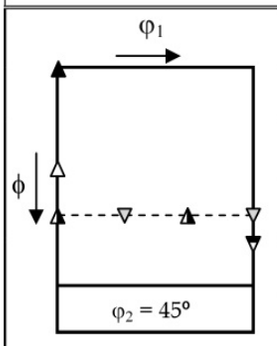


| {hkl} | <uvw> | φ1 | ϕ | φ2 |
|---|---|---|---|---|
| 001 | 110 | 0° | 0° | 45° |
| 112 | 110 | 0° | 35° | 45° |
| 111 | 110 | 0° | 54° | 45° |
| 111 | 112 | 30° | 54° | 45° |
| 554 | 225 | 90° | 60° | 45° |

**Table 3.** BCC rolling components.

## 3. Plasticity framework

We begin this section with the kinematic definitions of crystal-plasticity theory, citing the basic equations. The kinematic development of a single-crystal plasticity model has been well documented by several authors and is the subject of recent works (Kocks et al., 1998; Roters et al., 2010). Here we assume that, during plastic forming operations, it is possible to neglect the elastic contribution to deformation. Consequently, we will restrict ourselves to a rate-dependent plastic response at the single-crystal level.

### 3.1. Viscoplastic crystal plasticity

The velocity-gradient tensor, using a dot to indicate the time derivative, is given by

$$\mathbf{L} = \dot{\mathbf{F}} : \mathbf{F}^{-1} = \dot{\mathbf{R}}^{*} : \mathbf{R}^{*\mathrm{T}} + \mathbf{R}^{*} : \mathbf{L}^{\mathrm{p}} : \mathbf{R}^{*\mathrm{T}}. \tag{4}$$

In this expression, $\mathbf{R}^{*}$ represents the crystallographic rotation, $\mathbf{F}$ corresponds to the effect of dislocation slip on the crystal deformation and $\mathbf{L}^{\mathrm{p}} = \dot{\mathbf{F}}^{\mathrm{p}} : \mathbf{F}^{\mathrm{p}-1}$ is the plastic velocity gradient resulting from dislocation motion along specific planes and directions in the crystal (all potentially activated slip systems are labeled with the superscript $s$):

$$\mathbf{L}^{\mathrm{p}} = \sum_{s} \left( \mathbf{n}^{s} \otimes \mathbf{b}^{s} \right) \dot{\gamma}^{s}, \tag{5}$$

here $\dot{\gamma}^s$ represents the dislocation slip rates, $\mathbf{n}^s$ and $\mathbf{b}^s$ are the normal to the system´s or systems´ glide plane and the Burgers' vector, respectively. They define the symmetric $\mathbf{m}^s$ and the screw-symmetric $\mathbf{q}^s$ parts of the Schmid orientation tensor:

$$\mathbf{m}^s = \frac{1}{2}\left( \mathbf{n}^s \otimes \mathbf{b}^s + \mathbf{n}^s \otimes \mathbf{b}^s \right), \tag{6}$$

$$\mathbf{q}^s = \frac{1}{2}\left( \mathbf{n}^s \otimes \mathbf{b}^s - \mathbf{n}^s \otimes \mathbf{b}^s \right). \tag{7}$$

The dislocation slip rates are derived using a viscoplastic exponential law (Hutchinson, 1976):

$$\dot{\gamma}^s = \dot{\gamma}_0 \left| \frac{\mathbf{m}^s : \mathbf{S}}{\tau_c^s} \right|^{1/m} sign(\mathbf{m}^s : \mathbf{S}). \tag{8}$$

where $\dot{\gamma}_0$ is the reference slip rate, $\tau_c^s$ is the critical resolved shear stress on the slip system labeled *s*, **S** is the deviatoric tensor stress and *m* is the strain-rate sensitivity exponent. The rate sensitivity *m* is typically quite small, a large value of 1/*m* tends to be almost a rate independent case, ~ 50. As 1/*m* → ∞, the plastic constitutive formulation becomes formally rate-independent.

The velocity gradient can be additively decomposed into symmetric and skew-symmetric parts

$$\mathbf{L} = \mathbf{D} + \mathbf{W}, \tag{9}$$

where $\mathbf{D}$ is the distortion rate tensor and $\mathbf{W}$ is the rotation rate tensor. They can be obtained by evaluating the symmetric and screw-symmetric parts of equation (4), respectively:

$$\mathbf{D} = \mathbf{R}^* : \mathbf{D}^{\mathrm{p}} : \mathbf{R}^{*\mathrm{T}}, \tag{10}$$

$$\mathbf{W} = \boldsymbol{\Omega} + \mathbf{R}^* : \mathbf{W}^{\mathrm{p}} : \mathbf{R}^{*\mathrm{T}}. \tag{11}$$

The rotation rate contains an extra contribution, the lattice spin tensor, defined as $\boldsymbol{\Omega} \equiv \dot{\mathbf{R}}^* : \mathbf{R}^{*\mathrm{T}}$. Rearranging Eq. (11) allows us to obtain the rate of change of the crystal orientation matrix:

$$\boldsymbol{\Omega} = \mathbf{W} - \mathbf{R}^* : \mathbf{W}^{\mathrm{p}} : \mathbf{R}^{*\mathrm{T}}, \tag{12}$$

which is used to determine the re-orientation of the crystal and consequently, to follow the texture evolution. The orientation change during plastic deformation can be described by a list of the Euler angle change rates, $\left(\dot{\varphi}_1, \dot{\phi}, \dot{\varphi}_2\right)$, related to the lattice spin as follows:

$$\begin{aligned}\dot{\varphi}_1 &= \Omega_{13}\frac{\sin\varphi_2}{\sin\phi} - \Omega_{23}\frac{\cos\varphi_2}{\sin\phi} \\ \dot{\phi} &= -\Omega_{23}\cos\varphi_2 - \Omega_{13}\sin\varphi_2 \\ \dot{\varphi}_2 &= \cos\phi\left(\Omega_{13}\frac{\cos\varphi_1}{\sin\phi} - \Omega_{23}\frac{\sin\varphi_1}{\sin\phi}\right) + \Omega_{21}\end{aligned} \tag{13}$$

### 3.2. The 1-site VPSC-TGT formulation

For simulating the material response, a rate-dependent polycrystalline model is employed. In what follows, we present some features of the 1-site tangent VPSC-TGT formulation. For a more detailed description, the reader is referred to Lebensohn & Tomé (1993). This model is based on the viscoplastic behavior of a single crystal and uses a SC homogenization scheme for the transition to the polycrystal. Unlike the FC model, for which the local strain in each grain is considered to be equal to the macroscopic strain applied to the polycrystal, the SC formulation allows each grain to deform differently, according to its directional properties and the strength of the interaction between the grain and its surroundings. In this sense, each grain is in turn considered to be an ellipsoidal inclusion surrounded by a homogeneous effective medium, HEM, which has the average properties of the polycrystal. The interaction between the inclusion and the HEM is solved by means of the Eshelby formalism (Mura, 1987). The HEM properties are not known in advance; rather, they have to be calculated as the average of the individual grain behaviors, once a convergence is achieved. In what follows, we will only present the main equations of the VPSC model.

The deviatoric part of the viscoplastic constitutive behavior of the material at a local level is described by means of the non-linear rate-sensitivity equation:

$$\mathbf{D} = \dot{\gamma}_0 \sum_{s=1}^{\#sys} \mathbf{m}^s \frac{\mathbf{m}^s:\mathbf{S}}{\tau_c^s}\left|\frac{\mathbf{m}^s:\mathbf{S}}{\tau_c^s}\right|^{1/m-1} = \mathbf{M}:\mathbf{S}, \tag{14}$$

where $\mathbf{M}$ is the visco-plastic grain compliance. The interaction equation, which relates the differences between the micro and the macro strain rates $(\mathbf{D}, \bar{\mathbf{D}})$ and deviatoric stresses $(\mathbf{S}, \bar{\mathbf{S}})$, can be written as follows:

$$\mathbf{D} - \bar{\mathbf{D}} = -\alpha\tilde{\mathbf{M}}:(\mathbf{S} - \bar{\mathbf{S}}) \ . \tag{15}$$

The interaction tensor $\tilde{\mathbf{M}}$, which is a function of the overall modulus and the shape and orientation of the ellipsoid that represents the embedded grain, is given by:

$$\tilde{\mathbf{M}} = \left(\mathbf{I} - \mathbf{S}^{esh}\right)^{-1}:\mathbf{S}^{esh}:\bar{\mathbf{M}} \ , \tag{16}$$

where $\mathbf{S}^{esh}$ is the Eshelby tensor; $\mathbf{I}$ is the 4th order identity tensor, and $\bar{\mathbf{M}}$ is the macroscopic visco-plastic compliance. The parameter $\alpha$ tunes the strength of the interaction tensor. In the present models, the standard TGT approach is used ($\alpha = 1$).

The macroscopic compliance can be adjusted iteratively using the following self-consistent equation:

$$\bar{\mathbf{M}} = \langle \mathbf{M}:\mathbf{B} \rangle, \qquad \mathbf{B} = \left(\mathbf{M} + \tilde{\mathbf{M}}\right)^{-1} : \left(\bar{\mathbf{M}} + \tilde{\mathbf{M}}\right), \tag{17}$$

where $\langle\ \rangle$ denotes a weighted average over all the grains in the polycrystal, and $\mathbf{B}$ is the accommodation tensor defined for each single crystal. The solution is reached using an iterative procedure that involves Eqs. (14), (15) and (17). It gives the stress in each crystal, the local compliance tensor and the corresponding polycrystal tensor, which is consistent with the impose boundary conditions.

### 3.3. Marciniak and Kuczynski technique

For simulating formability behavior, we implemented the VPSC formulation described above in conjunction with the well-known MK approach. As originally proposed, the analysis assumes the existence of a material imperfection such as a groove or a narrow band across the width of the sheet. In the approach´s modified form, developed by Hutchinson & Neale (1978), an angle $\psi_0$ with respect to the principal axis determines the band's orientation (Fig. 4). Tensor components are taken with respect to the Cartesian $X_i$ coordinate system, and quantities inside the band are denoted by the subscript b.

The thickness along the minimum section in the band is denoted as $h_b(t)$, with an initial value $h_b(0)$, while an imperfection factor $f_0$ is given by an initial thickness ratio inside and outside the band:

$$f_0 = \frac{h_b(0)}{h(0)}, \tag{18}$$

with $h(0)$ being the initial sheet thickness outside the groove.

Equilibrium and compatibility conditions must be fulfilled at the interface with the band. Following the formulation developed by Wu et al. (1997), the compatibility condition at the band interface is given in terms of the differences between the velocity gradients $\left(\bar{\mathbf{L}}, \bar{\mathbf{L}}^b\right)$ inside and outside the band respectively:

$$\bar{\mathbf{L}}^b = \bar{\mathbf{L}} + \dot{\mathbf{c}} \otimes \mathbf{n}. \tag{19}$$

Eq. (19) is decomposed into the symmetric, $\bar{\mathbf{D}}$, and screw-symmetric, $\bar{\mathbf{W}}$, parts:

$$\bar{\mathbf{D}}^b = \bar{\mathbf{D}} + \tfrac{1}{2}\left(\dot{\mathbf{c}} \otimes \mathbf{n} + \mathbf{n} \otimes \dot{\mathbf{c}}\right), \tag{20}$$

$$\bar{\mathbf{W}}^b = \bar{\mathbf{W}} + \tfrac{1}{2}\left(\dot{\mathbf{c}} \otimes \mathbf{n} - \mathbf{n} \otimes \dot{\mathbf{c}}\right) \tag{21}$$

Here, $\mathbf{n}$ is the unit normal to the band, and $\dot{\mathbf{c}}$ is a vector to be determined. The equilibrium conditions required at the band interface are given by

$$\mathbf{n}.\bar{\boldsymbol{\sigma}}^{\mathrm{b}}\, h_{\mathrm{b}} = \mathbf{n}.\bar{\boldsymbol{\sigma}}\, h, \tag{22}$$

where $\bar{\boldsymbol{\sigma}}$ denotes the Cauchy stress. Noting that $\delta_{\mathrm{ij}}$ is the Kronecker symbol, the boundary condition $\bar{\sigma}_{33} = 0$ is applied as follows

$$\bar{\sigma}_{\mathrm{ij}} = \bar{\mathrm{S}}_{\mathrm{ij}} - \bar{\mathrm{S}}_{33}\, \delta_{\mathrm{ij}} \qquad (\mathrm{i} = 1,2,3)\,. \tag{23}$$

The integration of the polycrystalline model inside and outside the band is performed in two steps. First, an increment of strain is applied to the material outside the band, $\bar{\mathbf{D}}\, \Delta t$, while the imposed strain path on the edges of the sheet is assumed to be

$$\rho = \frac{\bar{\mathrm{L}}_{22}}{\bar{\mathrm{L}}_{11}} = \frac{\bar{\mathrm{D}}_{22}}{\bar{\mathrm{D}}_{11}} = \mathrm{const.} \tag{24}$$

It is assumed that $\bar{\mathrm{D}}_{13} = \bar{\mathrm{D}}_{23} = \bar{\mathrm{W}}_{13} = \bar{\mathrm{W}}_{23} = 0$ outside and inside the band. The instability appears in a narrow zone inclined at an angle $\psi_0$ with respect to the major strain axis. The equilibrium condition, Eq. (22), can be expressed in the set of axes referenced to the groove $\mathbf{n}, \mathbf{t}$ (see Fig. 4):

$$\begin{aligned} \bar{\sigma}^{\mathrm{b}}_{\mathrm{nn}}\, h_{\mathrm{b}} &= \bar{\sigma}_{\mathrm{nn}}\, h \\ \bar{\sigma}^{\mathrm{b}}_{\mathrm{nt}}\, h_{\mathrm{b}} &= \bar{\sigma}_{\mathrm{nt}}\, h. \end{aligned} \tag{25}$$

The compatibility condition requires equality of elongation in the direction $\mathbf{t}$,

$$\bar{\mathrm{D}}^{\mathrm{b}}_{\mathrm{tt}} = \bar{\mathrm{D}}_{\mathrm{tt}}\ . \tag{26}$$

Because, we are considering thin sheets with the orthotropic symmetries in the plane of the sheet in this research, in-plane stretching results in a plane-stress state. As discussed by Kuroda & Tveergard (2000), when an orthotropic material is loaded along directions not aligned with the axes of orthotropy, it is necessary to compute the $\bar{\mathrm{L}}_{12}$ component by imposing the requirement that $\bar{\sigma}_{12} = 0$. After solving each incremental step, the evolution of the groove orientation $\psi$ is given by

$$\mathbf{n} \;=\; \frac{1}{\sqrt{t_1^2 + t_2^2}} \begin{pmatrix} -\mathrm{F}_{11}\, t_1^0 - \mathrm{F}_{12}\, t_2^0 \\ \mathrm{F}_{21}\, t_1^0 + \mathrm{F}_{22}\, t_2^0 \end{pmatrix} \;\; ; \tag{27}$$

where $\mathbf{F}$ is the deformation gradient tensor.

The system of Eqs. (19) and (22, 23) can be solved to obtain $\dot{\mathbf{c}}$. This is done by substituting the macroscopic analogous Eq. (14) into the incremental form of Eq. (22) and using Eq. (20) to eliminate the strain increments in the band. At any increment of strain along the

prescribed strain path, the non-linear system of two equations is solved (Signorelli et al., 2009). More recently, in Serenelli et al. (2011), Eqs. (25) and (26) were used after obtaining the state ($\bar{\mathbf{L}}$, $\bar{\boldsymbol{\sigma}}$) in the homogeneous zone, in order to solve the groove state avoiding the 2x2 set of non-linear equations mentioned above. In this case, the remaining unknowns $\bar{L}^b_{11}, \bar{L}^b_{12}, \bar{L}^b_{33}$ and $\bar{\sigma}^b_{22}, \bar{\sigma}^b_{13}, \bar{\sigma}^b_{23}$ are obtained by solving a mixed boundary-condition in the VPSC module, with the logic time benefits.

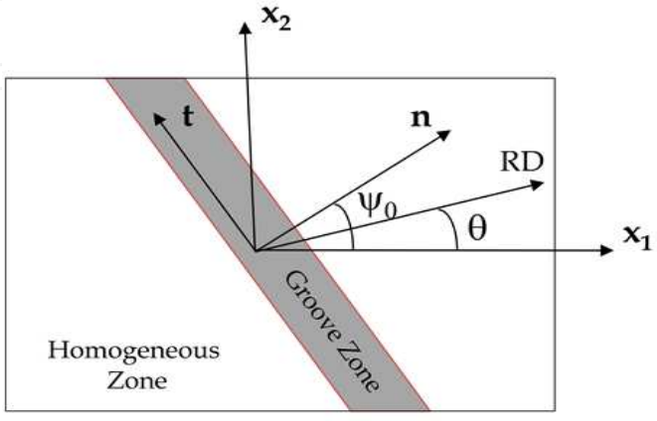


**Figure 4.** A thin sheet in the plane $x_1$-$x_2$ with an imperfection band.

To analyze the development of deformation localization during proportional straining, the calculations were performed over different strain paths. They were defined in terms of the strain-rate ratios $\rho = \bar{D}_{22} / \bar{D}_{11}$ over the range -0.5 ≤ ρ ≤ 1 (step = 0.1). The possible variations of the FLD for each ρ are obtained by performing calculations every 5 degrees of $\Psi_0$ to a maximum of 90 degrees. The failure strains $\varepsilon^*_{11}$, $\varepsilon^*_{22}$ outside the band and the critical failure angle $\Psi^*$ are obtained after minimizing the curve $\varepsilon^*_{11}$ versus $\Psi_0$. In the present work, failure is assumed when $\left|\bar{D}^b_{33}\right| > 20\left|\bar{D}_{33}\right|$.

## 4. Effects of the main model´s parameters on the FLDs

In this section, we analyze the influences on the limit strains of the initial-imperfection intensity and orientation, the strain-rate sensitivity and the hardening to determine MK-VPSC performance. The sensitivity of the MK-VPSC model to the initial grain-shape and to texture and textural evolution is also addressed, by showing results obtained from sheets with rolling and random initial textures. In this section, the material inside and outside of the groove is taken to be a polycrystal described by 1000 equiaxed grains, except where noted otherwise. Each grain is assumed to be a single crystal with a FCC crystal structure. Plastic deformation occurs on 12 crystallographic slip systems of the type {111}<110>. We constructed the initial texture in both zones to be the same, and assumed a reference plastic shearing rate of $\dot{\gamma}_0$ = 0.001 $s^{-1}$. In order to account for the strain hardening between slip systems, we adopted isotropic hardening. In this case the evolution of the critical shear stresses is given by

$$\dot{\tau}_c = \sum_s h^s \left| \dot{\gamma}^s \right| \tag{28}$$

where $h^s$ are the hardening moduli behaviors, which depend on $\Gamma$ (accumulated sum of the single-slip contributions to $\gamma^s$). These moduli can be written using the initial hardening rate, $h_0$, and the hardening exponent, $n$:

$$h^s = h_0 \left( \frac{h_0 \Gamma}{\tau_c^s n} + 1 \right)^{n-1} ; \qquad \Gamma = \sum_s \int_0^t \left| \dot{\gamma}^s \right| dt \, . \tag{29}$$

The strain-induced hardening law prescribed above is applied to all slip systems.

## 4.1. Initial imperfection

The MK approach predicts the FLD based on the growth of an initial imperfection. However, the strength of the imperfection cannot be directly measured by physical experiments. Zhou & Neale (1995) analytically predicted the effect of the initial imperfection parameter $f_0$ on the FLD and demonstrated, as expected, that the forming-limit strain decreases with increasing depth of the initial imperfection. Using the MK-VPSC approach, we too determined that the limit strains are greatly affected by the value of $f_0$. In addition, we found, as did Zhou & Neale, that the smaller the imperfection the larger the limit strain. The calculations plotted in Fig. 5 were performed using a random initial texture.

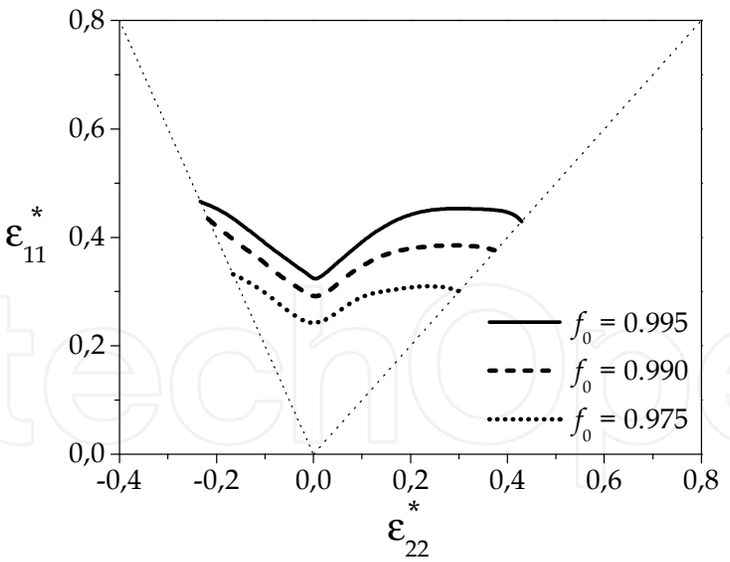


($m$ = 0.01, $n$ = 0.23, $h_0$ = 1410 MPa, $\tau_c^s$ = 47 MPa).

**Figure 5.** Influence of the initial imperfection $f_0$ on the FLD

All three curves show the minimum limit strain close to the in-plane plane-strain path. Although the limit strains are different for the different values of the initial imperfection, the profiles of the simulated cases are equivalent over the range $-0.5 \leq \rho \leq 0.3$. For $\rho > 0.3$, the

profiles of the FLD curves remain insensitive to defect severity, except for paths approaching equal-biaxial deformation. In this case, the largest value of $f_0$ gives a more pronounced fall in the limit strain. Our results compare favorable to those of Wu et al. (1997), but these authors predict a more noticeable decrease of the limit-strains as the strain path approaches ρ = 1.0. It is possible that the FC homogenization scheme used by Wu et al., rather than the SC scheme of the present work, produced these differences. Also, we assumed a greater strain-rate sensitivity than did Wu and his co-authors. As we will see in the next section, larger rate sensitivities produce higher limit-strain profiles near ρ = 1.0.

## 4.2. Strain-rate sensitivity

The influence of the material's rate sensitivity $m$ on the FLDs is addressed. Fig. 6 shows the calculated limit-strains assuming a random initial texture and an initial imperfection of $f_0$ = 0.99. Depending on the $m$ value, not only are the limit strains different, but the FLD profiles vary as well. The limit-strains decrease with decreasing $m$, for $m$-values of 0.05, 0.02 and 0.01, while the FLD profiles in the negative minor-strain range (ρ < 0) continue to exhibit a nearly linear behavior. For biaxial paths (ρ > 0) near plane strain, the forming-limit strain increases rapidly for low values of $m$, while for high $m$, $m$ = 0.05, the major limit-strain is nearly constant. As illustrated by the curves shown in Fig. 6, high values of $m$ also displace the ending of the steep-slope profile towards an equi-biaxial path. Analyzing the results for $m$ = 0.01 in the neighborhood of ρ = 1.0, we find decreasing limit-strains, indicating that lowering the strain-rate sensitivity produces a similar effect to that found using a Taylor model.

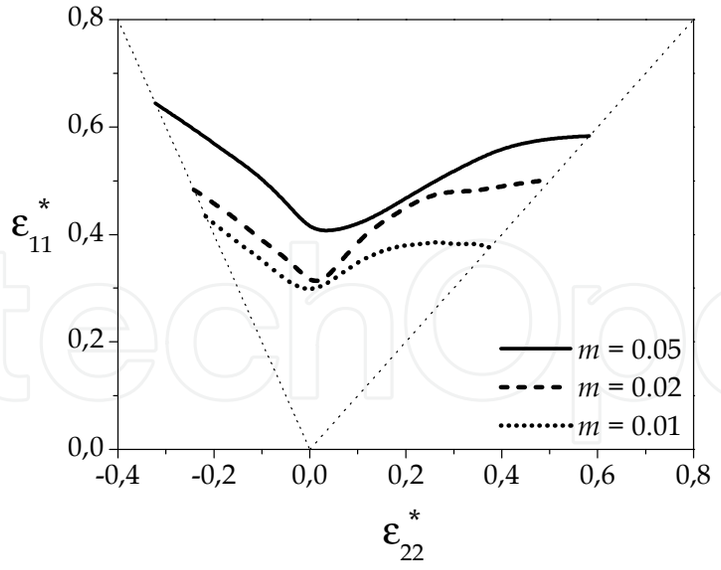


($f_0$ = 0.99, $n$ = 0.23, $h_0$ = 1410 MPa, $\tau_c^S$ = 47 MPa).

**Figure 6.** Influence of the rate sensitivity $m$ on the FLD

The effects produced by the different strain-rate sensitivities are consistent with the relationship between the hardening behavior and $m$, described by Eqs. (28) and (29). The

parameter *m* in the viscoplastic law controls the accumulated shear, which in turn drives the hardening. It is also known that as the *m* value increases textural sharpness decreases, though this behavior depends on the imposed strain path, too. The calculated average number of slip systems associated with the main strain paths and several additional material sensitivities are presented in Table 4. It is interesting to note that, as expected, the fewer the number of slip systems and the sharper the texture the lower the limit curve.

| | $m = 0.05$ | $m = 0.02$ | $m = 0.01$ |
|---|---|---|---|
| $\rho = -0.5$ | 4.5 | 2.8 | 2.3 |
| $\rho = 0.0$ | 2.8 | 2.2 | 1.9 |
| $\rho = 1.0$ | 3.3 | 3.1 | 2.8 |

**Table 4.** Calculated average number of active slip systems as a function of the deformation path and strain-rate sensitivity.

As opposed to the results for the limit-strain values, the critical angles at failure are almost insensitive to the strain-rate sensitivity. The predicted final angles rise to between $\Psi^* = 34°$-37° for a uniaxial path and decrease to zero degrees for $\rho \geq 0$. If we restrict the model interaction to the FC hypothesis, as done by Wu et al. (1997), our calculated values equal theirs.

### 4.3. Hardening coefficients

Slip induced hardening is another important factor influencing the limit strains. From Eqs. (28) and (29) it is easy to see that the parameters $h_0$ and $n$ govern the strain hardening. We investigated the effect produced by different values of the hardening coefficient $n$ (0.16, 0.19 and 0.23) while fixing the other material properties. The calculated FLDs are shown in Fig. 7, where it is clear that the slip hardening coefficient $n$ does not affect the shape of the forming limit curves. However, it can be seen that the largest value of $n$ produces the highest limit strains. Also, no noticeable dependence with $\rho$ is observed. Because we use isotropic hardening in these calculations, the $n$ parameter only guides the stress level, producing these simple behaviors. This will not be the case when latent hardening and other kinematic effects are included in the calculations.

### 4.4. Grain shape

It is important for the reader to note that the VPSC model has the capability to account for the grain-shape and its evolution. The influence of different elongated grain-shapes on the limit strains is shown in Fig. 8 for a non-textured material. Generally, the calculated FLDs decrease when increasingly elongated grains are considered. In the negative minor-strain range, no appreciable changes are noted in the FLD's behavior for different aspect ratio grains. To the contrary, in the biaxial-stretching zone, differences are observed, especially when the aspect ratio is more pronounced. For initially equiaxed grains and grains elongated up to an aspect ratios of (3:1:1), the profiles of the simulated limit strains show no significant changes. However, for a (10:1:1) grain aspect ratio, we found a noticeable decrease of the limit-strains moving from plane-strain to equi-biaxial tension. This result can

be correlated with the final textures predicted for each grain-shape morphology. The {111} pole figures calculated for the homogeneous deformation zone at the end of the equi-biaxial loading path are shown on the right in Fig. 8.

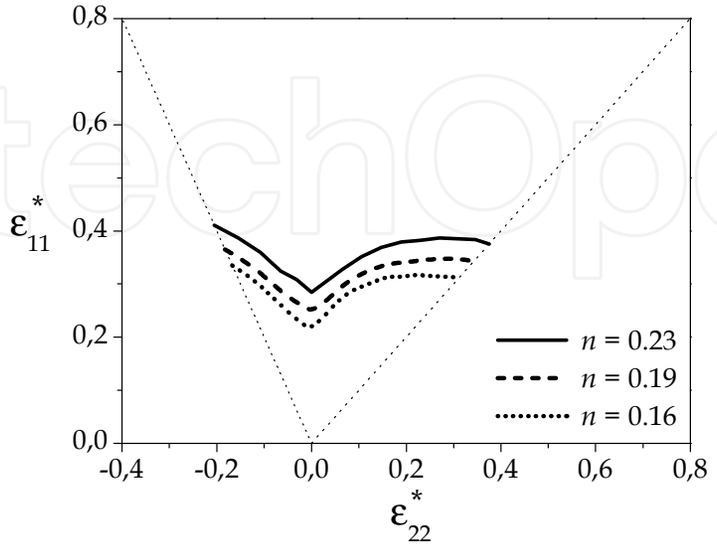


($f_0$ = 0.99, $m$ = 0.01, $h_0$ = 1410 MPa, $\tau_c^s$ = 47 MPa).

**Figure 7.** Influence of the slip-induced hardening $n$ on the FLD

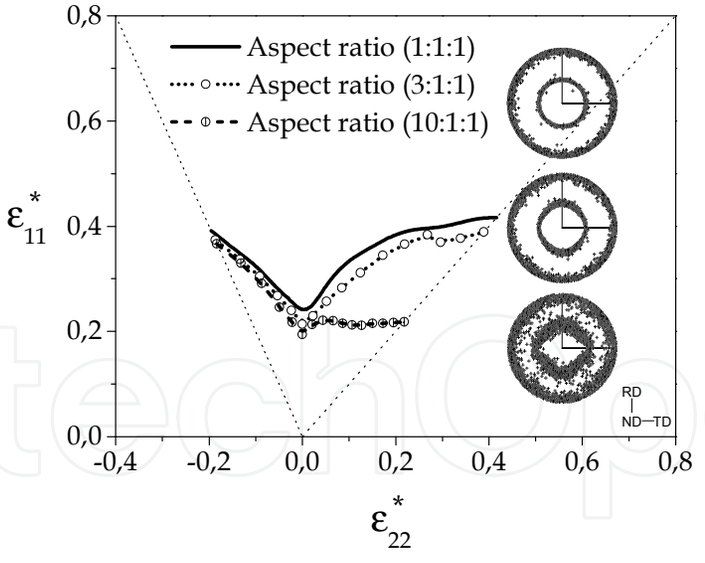


($f_0$ = 0.99, $m$ = 0.02, $n$ = 0.16, $h_0$ = 4000 MPa, $\tau_c^s$ = 22 MPa).

**Figure 8.** Influence of the initial grain shape on the limit-strains for a non-textured material

## 4.5. Effects of texture

A crystallographic texture develops during metal forming and it is a key component of the material's microstructure. It is generally accepted that this microstructural feature

significantly affects forming-limit strains. To investigate these texture effects, we carried out simulations using two initial textures: one a random distribution of orientations (R) and the other a rolling texture (S). Two {111} pole figures illustrating these textures are shown in Fig. 9. To construct the S texture we first fixed the ideal component volume fractions, 10% {001}<100>, 15% {011}<100>, 30% {123}<634>, 10% {112}<111> and 35% {011}<211>, and then spread the distribution by assigning each grain a misorientation angle of $\theta < 15°$ with respect to the ideal component.

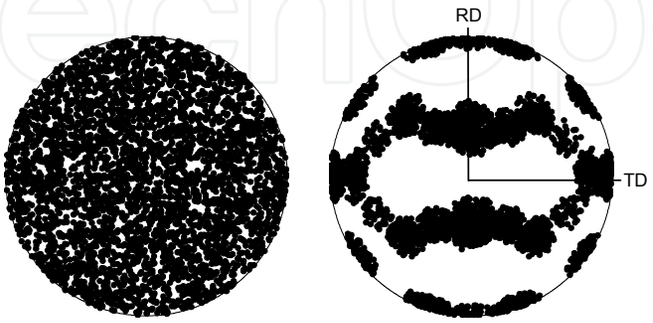


**Figure 9.** Grain orientation distributions represented by {111} pole figures: material R (left) and material S (right).

These different initial textures strongly affected the forming-limit curves as plotted in Fig. 10. In the negative minor-strain range ($\rho < 0$) of the FLD, the shapes are nearly straight lines with the maximum values at $\rho = -0.5$. The predictions, however, begin to diverge at $\rho = 0$, and the differences increase continuously, reaching a maximum for a biaxial deformation path. The S textured material develops a much stronger anisotropy than the R, likely producing the observed results. The S material's forming-limit curve slopes downwards from plane-strain to equi-biaxial tension, and over the whole range $\rho > 0$ the predicted forming limits for the R case are larger than those for the S. Fig. 10 includes a plot of the final textures of each sample at the end of the equi-biaxial loading path. Clearly, the R and S textures evolve to different states producing the strong effects observed in the FLD behavior.

Our calculations also show that the influence of crystallographic texture evolution is at least as important as effects of the initial grain distributions. Evolution effects have been previously discussed by several authors. Tóth et al. (1996) performed simulations with a rate independent Taylor model, showing that crystal rotations decrease the limit strains. Tang & Tai (2000), using the MK analysis together with continuum damage mechanics (CDM) and the Taylor model, found the same behavior for the limit strains. They claim that the development of texture causes deterioration of the material. On the other hand, Wu et al. (2004b) use a mesoscopic approach and a Taylor homogenization scheme to show that texture evolution increases the limit-strains in the biaxial zone. Finally, Inal et al. (2005) recently analyzed these two studies and their opposite conclusions, adding a study of how texture evolution in BCC materials affects the FLD. In the work of Inal et al., the simulations show that texture development does not have a significant influence on the FLD. Actually based on our simulations, we found it necessary to analyze the development of material

anisotropy in a more complex way in order to determine the effect of texture updating on the limit strains. This in turn is captured more or less realistically by the different homogenization schemes.

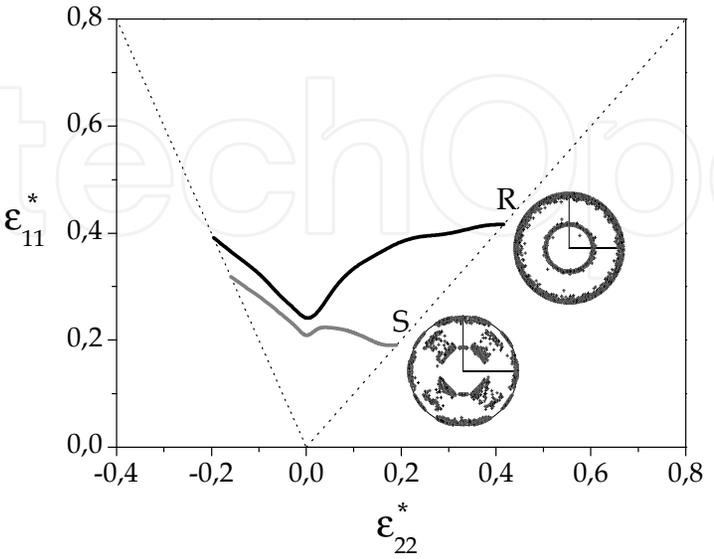


($f_0$ = 0.99, $m$ = 0.02, $n$ = 0.16, $h_0$ = 4000 MPa, $\tau_c^s$ = 22 MPa).

**Figure 10.** Influence of the initial texture on the FLD

Such an analysis can explain the opposite trends in limit strains reported by previous researchers, which cannot be understood based only on initial-material textures. In our opinion, the differences in the forming-limit strains are related to material anisotropy and its evolution along the deformation path. This produces an increase or decrease of the FLD profile. Many previous investigations have proven that the VPSC model gives a more realistic description of the anisotropic behavior of polycrystalline materials. We believe that results of the MK-VPSC strategy presented here are a better way to explain and justify the different effects of the material parameters.

To assess the influence of the texture evolution on the limit strains, we repeated the calculations shown in Fig. 10 but without texture evolution (Fig. 11). In negative strain space ($\rho < 0$) the FLDs have practically identical shapes, although the calculated values are slightly lower when the initial texture is not updated. However, in the biaxial zone, the tendency is quite different. The FLDs for both materials now approach each other, and a certain matching is observed. For the R texture, the limit-strain values reflect texture evolution. Texture and hence anisotropy evolution produces greater limit strains. In the case of the S material, when texture updating is off, the limit strains in the biaxial zone increase continuously, showing a different behavior than when the texture is updated. We attribute this behavior to the sharpness of the material yield locus and consequently, to the slip systems selected to accommodate the imposed deformation. The corresponding yield-loci after equi-biaxial stretching for both materials are displayed in Fig. 12 in $\sigma_{11} - \sigma_{22}$ space. Following Barlat's work (1989), the parameter $p$ quantifies the effect of yield-surface shape

on limit strains for the last four cases (Table 5). It should be noted that the trends of $p$ and the predicted limit-strain values are consistent, as Hiwatashi et al. (1998) and Friedman & Pan (2000) have noted.

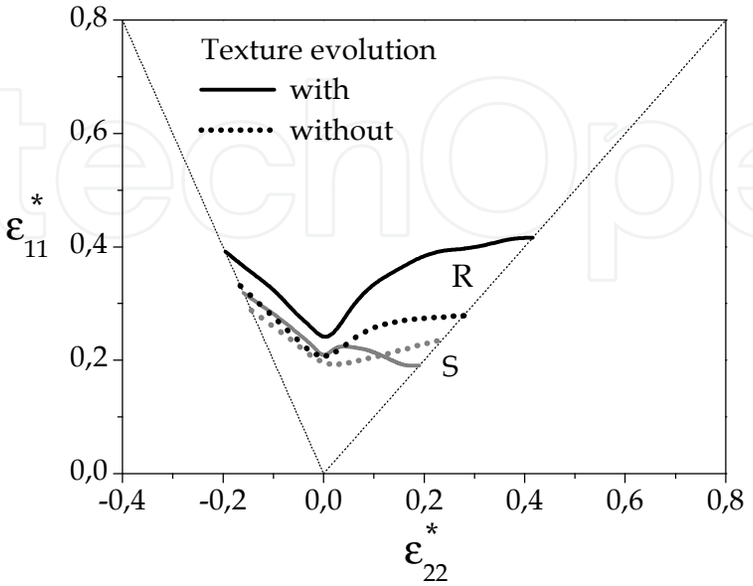


($f_0 = 0.99$, $m = 0.02$, $n = 0.16$, $h_0 = 4000$ MPa, $\tau_c^s = 22$ MPa).

**Figure 11.** Influence of texture evolution on the FLD

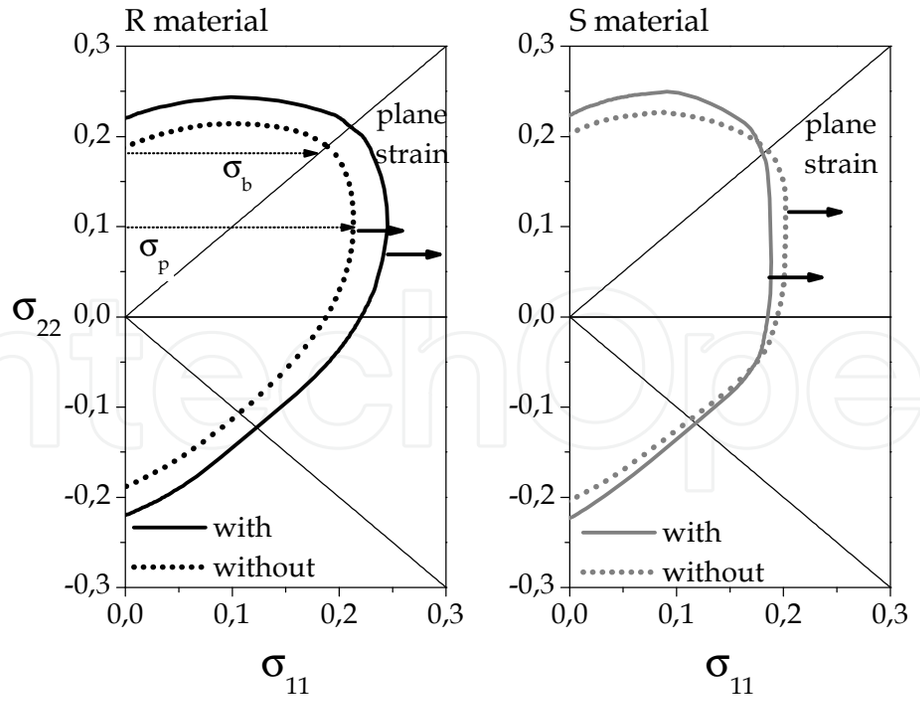


**Figure 12.** Calculated yield loci for materials R and S with (solid lines) and without (dotted lines) texture evolution. The equi work-rate surface is normalized to the work rate for uniaxial stretching, as calculated with the FC model.

| Material | Texture evolution | $p$ |
|---|---|---|
| R | Yes | 1.159 |
| S | No | 1.072 |
| R | Yes | 1.131 |
| S | No | 1.087 |

**Table 5.** $p$-parameter for the R and S equi-biaxial stretching cases.

## 5. Discussions about MK–FC and MK–VPSC approaches

A comparison between the FC and the VPSC interaction models is the subject of this section. For this purpose, we calculate forming-limit strains using both homogenization schemes together with the MK approach. The numerical procedure, previously applied to a FCC structure, is extended to include the slip-system families of BCC polycrystals. The consequences of the FCC and BCC crystallographic-slip assumptions, coupled with the selection of either FC or SC type grain-interactions, are investigated in detail. Then, we focus on the effect of the cube texture on the forming-limit behavior, and seek to explain why a spread about cube exhibits unexpectedly high limit strains close to equi-biaxial stretching when the MK-FC is used. Finally, we explore the right-hand side of the FLD for a BCC material considering either 24 or 48 active slip systems for crystal-plasticity simulations. The advantages of using the VPSC material model in the MK approach are discussed at the end of this section. For all calculations in this section, and as was pointed out in Section 4, the strain hardening between slip systems is taken into account by adopting isotropic hardening.

In what follows, we apply the MK-VPSC and MK-FC approaches for predicting FLDs to both FCC and BCC materials. We assume that plastic deformation occurs by 12 crystallographic slip systems of the type {111} <110> for the FCC material and 48 slip systems of the type {110} <111>, {112} <111> and {123} <111> for the BCC. The crystal level properties listed in Table 6 are determined by imposing the same uniaxial behaviors for all simulations. An initially random texture, described by 1000 equiaxed grains is assumed. The slip resistances $\tau_c^s$ of all slip systems are taken equal, the rate sensitivity is $m$ = 0.02, and a reference slip rate of $\dot{\gamma}_0$ = 0.001 s$^{-1}$ is assumed.

| **Material** | **FCC-FC** | **FCC-SC** | **BCC-FC** | **BCC-SC** |
|---|---|---|---|---|
| $h_0$ (MPa) | 1950 | 2720 | 1850 | 3100 |
| $n$ | 0.250 | 0.224 | 0.250 | 0.265 |
| $\tau_c^s$ (MPa) | 31.5 | 47.0 | 37.0 | 45.0 |

**Table 6.** Material parameters used in the simulations.

To analyze the development of deformation localization during proportional straining, the calculations are performed assuming an initial imperfection of $f_0$ = 0.99 over the different strain paths. The predicted limit strains are presented in Fig. 13. For each homogenization method, both materials have about the same profile from uniaxial tension (ρ = -0.5) to in-

plane plane-strain tension (ρ = 0). Over this entire range, the major limit strains decrease with increasing ρ. It can be seen that, for the BCC-SC material, the largest value of the parameter *n* results in the highest limit values. Also, it is interesting to note that MK-FC simulations using the same *n* value predict similar limit strains for the in-plane plane strain condition.

Predictions begin to diverge in the biaxial-stretching range. Here, results clearly illustrate large differences between the homogenization schemes and between materials. These differences reach a maximum for the equi-biaxial deformation path. The MK-FC framework predicts both the highest and lowest limit strains, for the BCC and FCC materials respectively. The MK-FC FCC material calculation leads to a remarkably low limit curve. Completely the opposite behavior is observed within the MK-VPSC scheme. In this case, the FCC material shows better formability than the BCC for ρ ≥ 0.3, and for both materials, the calculated limit-strain curves remain between those calculated with the MK-FC scheme near the equi-biaxial zone. In the case of the FCC material, the MK-VPSC approach predicts a noticeable increase of the limit strains over the whole right side of the diagram, while the BCC material only shows that behavior in the region 0 ≤ ρ ≤ 0.6. For ρ ≥ 0.6, the MK-VPSC limit-strain values are nearly constant. Fig. 13 also includes the {100} stereographic pole figures of each material at the end of the equi-biaxial stretching path. As can be seen, FCC and BCC material textures evolve differently depending on the model assumption. For a FCC material, the FC model develops a weaker texture than that produced by the VPSC calculation. For the BCC case, the final textures are qualitatively similar but quantitatively different in their degree of intensity.

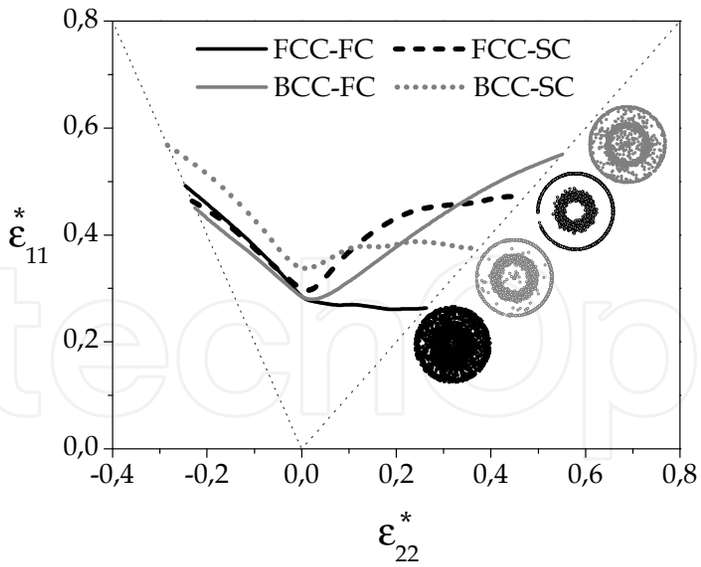


**Figure 13.** Influence of the slip microstructure and interaction model on the FLD.

According to Lian et al. (1989), the yield-surface shape has a tremendous effect on the FLD, and Neale & Chater (1980) demonstrated that a decrease in the sharpness of the stress potentials in equi-biaxial stretching promotes larger limit strains. A sharp curvature allows the material to quickly select a deformation path approaching plane strain, and this results

in the prediction of a relatively low limit strain. The yield potentials of the materials were calculated by imposing different plastic strain-rate tensors under a state of plane stress in $\sigma_{11} - \sigma_{22}$ space. With the simulation, we deformed the material in equi-biaxial stretching up to a given plastic strain and then performed the yield-locus calculations. For the purpose of comparing polycrystal yield surfaces, all work-rates were normalized to that of FCC-FC uniaxial stretching. We calculated the yield loci corresponding to each of the necking limit strains, in order to highlight the link between the yield-surface shape and the forming-limit behavior. Shapes and curvatures predicted by the FC and VPSC models are shown in Fig. 14.

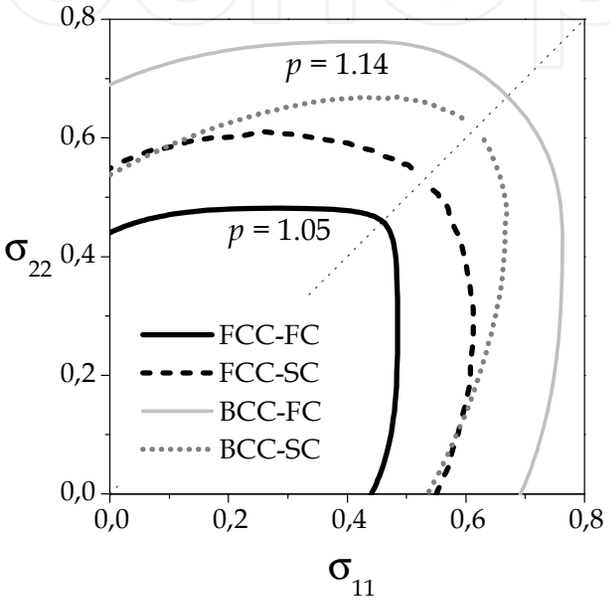


**Figure 14.** Calculated yield loci at equi-biaxial failure for all tested materials.

As expected, the curvature of the yield locus of the FCC-FC material in the equi-biaxial stretching zone is much sharper than those of the other materials, which is consistent with its limit-strain value, lowest among the cases considered, shown in Fig. 13. Similarly, the curvature of the BCC-FC yield locus is rounder than the others, which is again in agreement with the predicted limit strains. We also calculated the parameter $p$ for our materials finding that the values of $p$ for the FCC-FC and BCC-FC materials are the lowest and the highest, respectively.

The FLD results depend on the homogenization scheme, and the differences are explained in terms of the sharpness of the yield-loci and texture development. The MK-FC framework predicts both the highest and lowest limit strains, for the BCC and FCC materials respectively.

## 5.1. Influence of cube texture on sheet-metal formability

As mentioned in section 2.2, in rolled FCC sheets, crystallographic textures are frequently classified in terms of the ideal rolling and recrystallization components. Such classifications are well suited for theoretical modeling where mathematical descriptions of particular

components can be input into simulations. In particular, we focus on how the strength of the cube texture affects localized necking. To investigate this effect, we modeled variations of the cube texture. The variations were constructed with different spreads of grain orientations around the ideal cube component. The procedure for modeling textures is the same as that used in Signorelli & Bertinetti (2009). As an example, the cube-15° texture is one whose grains have a misorientation with respect to the ideal cube orientation {100}<001> of less than 15°, uniformly distributed over that area. Fig. 15 shows the {111} stereographic pole figures for cube-3°, cube-7°, cube-11° and cube-15° distributions. For the cube set of textures, the number of individual orientations was set in order to obtain an adequate representation of a uniform distribution.

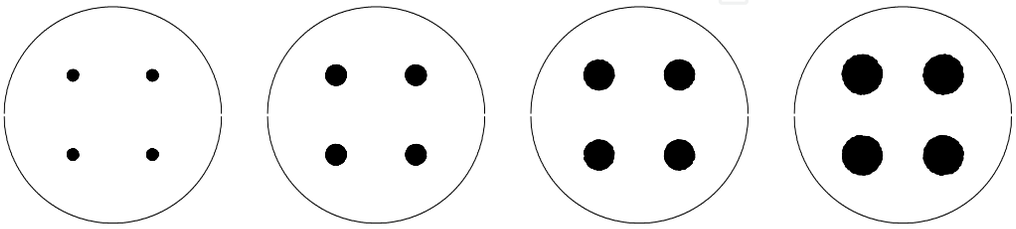

**Figure 15.** {111} pole figures used in the simulations for cube-3°, cube-7°, cube-11° and cube-15° distributions.

In the following FLD simulations, in both the homogeneous and MK band zones, standard FCC {111}<110> crystal slip is used, and the initial textures are assumed to be the same. Fig. 16 shows the predicted limit strains for the cube set of texture distributions using the MK-FC and MK-VPSC approaches. The simulations clearly show that there are differences between the VPSC and FC homogenization schemes, although the shapes and levels of the predicted FLDs are similar in the uniaxial range. No significant differences were found between the ideal cube and the cube-3° textures, since for this case the HEM nearly corresponds that of a single crystal. In these cases, both models closely predict shape and tendency. In the negative minor-strain range ($\rho < 0$) of the FLD, the shapes are nearly straight lines with the maximum values at $\rho = -0.5$. For both textures, the FLD curves slope downwards from plane-strain tension to equi-biaxial stretching, with the minimum limit-strain values at $\rho = 1$. These values are far below that of the random texture.

We would expect that a spread around the ideal orientation would give greater formability and higher limit strains. The FLD calculated from the random texture should be above all others, with the FLDs of particular spreads lying between those of the ideal cube and the random cases. Wu et al.'s (2004a) results do not show this expected behavior; their calculated forming-limit curves for cube-11° and cube-15° are significantly higher than that of the random texture near equi-biaxial stretching. These results were confirmed by Yoshida et al. (2007) using the same modeling hypothesis. Our simulations are similar to those reported by Wu et al. when the MK-FC approach is used. To the contrary, FLDs calculated with the MK-VPSC approach behave as expected. For $0 < \rho \leq 1$, the limit strains move upwards with an increase in the dispersion cut-off angle, and the strain-limit values never reach those of the random case.

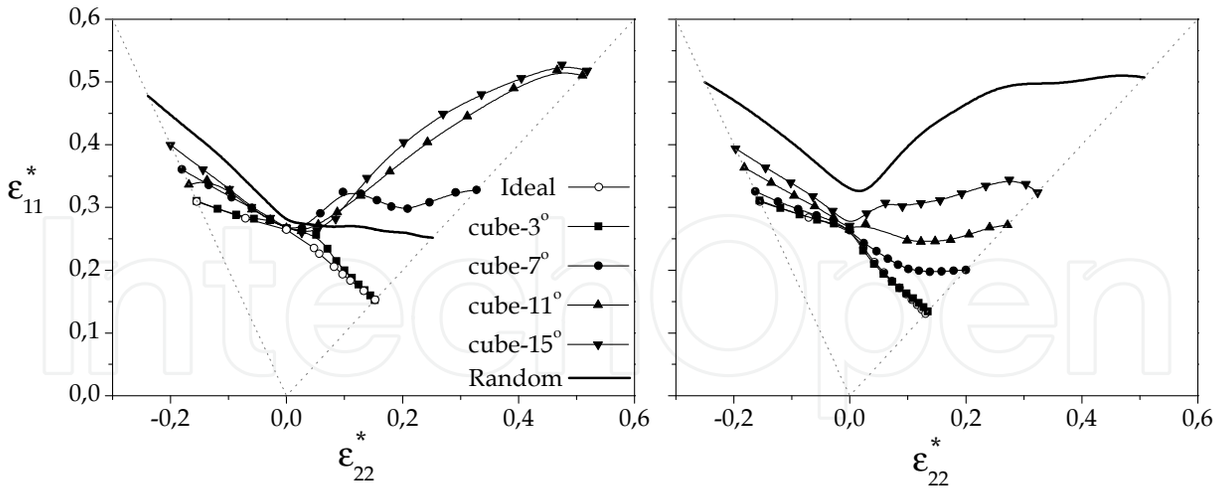


($f_0 = 0.99$, $m = 0.02$, $n = 0.24$, $h_0 = 1218$ MPa, $\tau_c^s = 42$ MPa).

**Figure 16.** Calculated FLDs for MK-FC (left) and MK-VPSC (right) models

In order to assess the effect of the yield-surface shape on the forming-limit behavior close to the balanced-biaxial stretching zone, ρ = 1.0, we prestrained the texture sets along the equi-biaxial path. The amounts of equi-biaxial strain corresponded to the necking-limit strains. Then, we calculate the yield-loci for cube-11°, cube-15° and random cases, using FC and VPSC models. The corresponding $\sigma_{11} - \sigma_{22}$ projections are shown in Fig. 17. The equi work-rate surfaces are normalized to the work rate for uniaxial stretching as calculated with the FC model. As expected, the yield loci are quite different. The curvatures of the VPSC yield loci are blunter than those of FC model, particularly for the random texture. This explains the higher limit-strains predicted by the MK-VPSC model as shown in Fig. 16. For the cube-11° and cube-15° initial textures, the FC yield loci are sharper and larger. As other researchers concluded and our simulations confirm, regions of reduced yield-locus curvature correspond to lower FLD values.

Fig. 18 shows the initial and final (at failure) inverse pole figures of the cube-15º for both constitutive-model approaches at ρ = 1.0. We found that the behavior of certain crystallographic orientations depends on the interaction model used. Particularly, near the <100> orientation, results of the models diverge. Using the VPSC approach, no grains remain close to <100> (Θ < 5º), but for the FC simulations this is not the case, and the grains rotate in widely different directions. In both cases, one can trace an imaginary line that delineates a zone containing a high density of orientations and one vacant of orientations. The grain orientations tend to rotate and accumulate in the region approximately defined by <115> - <114> and <104> - <102> for FC and by <116> - <115> and <104> - <305> for VPSC, respectively. In addition, we found that the FC final orientations are distributed rather uniformly in the inhabited region. Interestingly, for the VPSC calculations, there is a preference to rotate half-way up the <104> - <305> segment line. Similar behavior can be found for the cube-11º distribution.

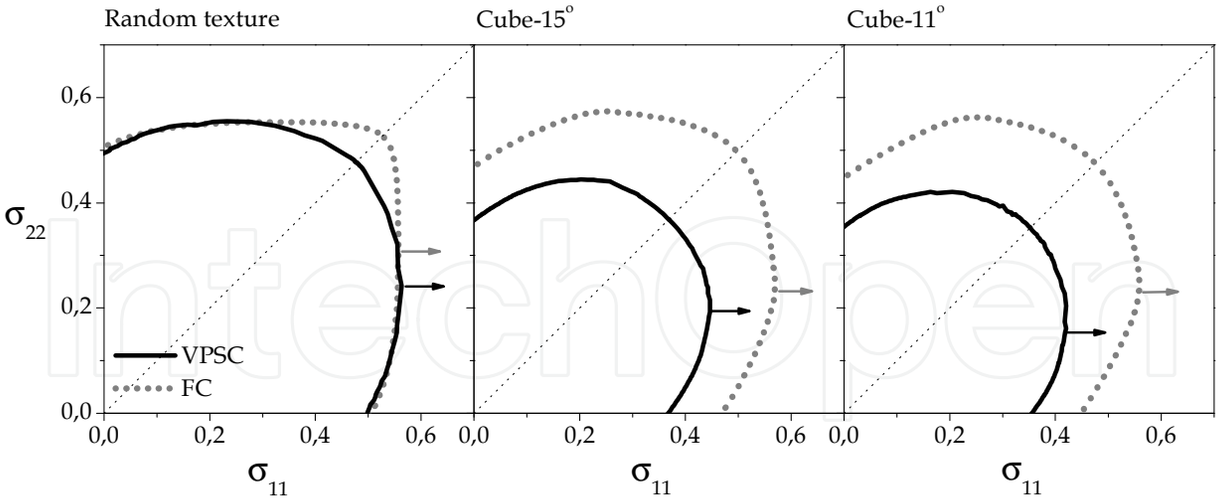


**Figure 17.** Calculated yield loci for VPSC and FC models. The equi work-rate surfaces are normalized to the work rate for uniaxial stretching, as calculated with the FC model.

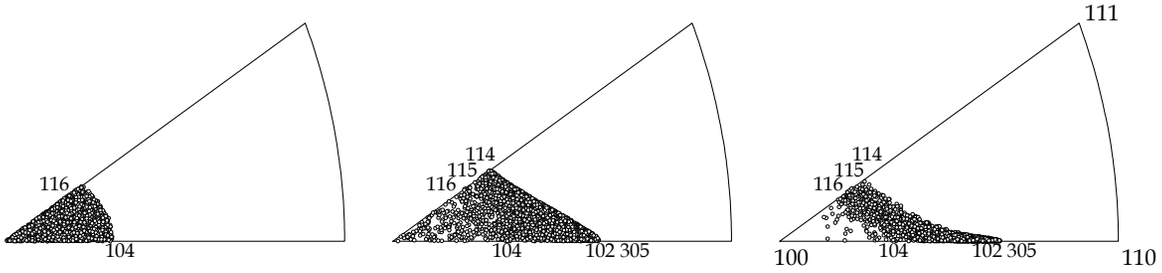


**Figure 18.** Stereographic triangles showing the initial cube-15° texture (left) and predicted final orientations after equi-biaxial stretching to failure by FC (center) and VPSC (right) models.

Simulations of FLDs show that the MK-FC strategy leads to unrealistic results, since an increasing spread about the cube texture produces unexpectedly high limit strains. However, results with the MK-VPSC approach successfully predict a smooth transition in the limit strains from the ideal-cube texture, through dispersions around the cube texture with increasing cut-off angles, ending with a random texture.

## 5.2. Influence of the dislocation slip assumption on the formability of BCC sheet metals

The identification of the active slip systems is a widely discussed issue in the plastic deformation of BCC crystals. The most common deformation mode is {110}<111>, but BCC materials also slip on other planes, {112} and {123}, with the same slip direction. In the literature, it is common for two sets of possible slip systems describing BCC plastic behavior to be considered: {110}<111>, {112}<111> (BCC24); or {110}<111>, {112}<111>, {123}<111> (BCC48). In what follows, we explore the right-hand side of the FLD for a BCC material using the proposed MK-FC and MK-VPSC approaches, and test the crystallographic slip assumption.

The crystal level properties are determined, by imposing same uniaxial behaviors for all the cases: BCC48-FC, BCC24-FC, BCC48-SC and BCC24-SC. Accordingly, the hardening parameters are chosen to give an identical uniaxial-stress response. They are listed in Table 7. The initial texture, the reference plastic shearing rate and shear strain-rate sensitivity are the same as used in the previous section.

| **Material** | **BCC48-FC** | **BCC48-SC** | **BCC24-FC** | **BCC24-SC** |
|---|---|---|---|---|
| $h_0$ (MPa) | 808 | 808 | 795 | 980 |
| $n$ | 0.23 | 0.26 | 0.23 | 0.26 |
| $\tau_c^s$ (MPa) | 30.5 | 40.0 | 30.0 | 37.0 |

**Table 7.** Material parameters used in the simulations.

The predicted limit strains are shown in Fig. 19. Large differences are between the MK-FC and MK-VPSC results, particularly near equi-biaxial stretching, regardless of the material. For each homogenization method, both materials have about the same forming limit in plane strain. At ρ = 0, we found no difference in the predicted limit-strains values given by either the BCC24 or BCC48 approach, but a discrepancy appears between the FC and SC polycrystal models. Within the MK-VPSC framework, the profiles of the BCC48 and BCC24 simulations are very close for the strain ratios ρ ≤ 0.6, and differences can be seen near equi-biaxial stretching. The MK-FC limit strains are similar as ρ increases up to 0.8, but for ρ > 0.8, the critical values calculated with the BCC24 deformation model increase to an unrealistic high value at ρ = 1. Our simulations clearly show that in equi-biaxial stretching the exclusion of {123}<111> crystallographic slip as a potential active deformation mode promotes higher limit strains for both models. For MK-VPSC this gap is only an increase in the limit strain from 0.37 to 0.39; whereas for MK-FC the value changes from 0.53 to 0.97.

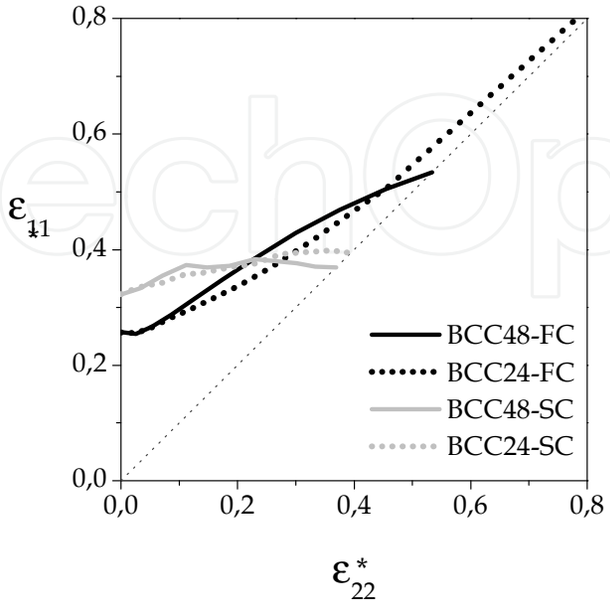


**Figure 19.** Influence of the slip microstructure and interaction model on the FLD.

The yield potentials of the materials were calculated by imposing different plastic strain-rate tensors under a state of plane stress in the $\sigma_{11} - \sigma_{22}$ section. With the simulation, we deformed the material in equi-biaxial stretching up to a given plastic strain and then performed the yield-locus calculations. For the purpose of comparing polycrystal yield surfaces, all work-rates were normalized to the case of BCC48-FC uniaxial stretching. We calculated the yield loci corresponding to each of the necking limit strains, in order to highlight the effect of the yield-surface shape on the forming-limit behavior. Particular attention must be paid to the surface's curvature near the balanced-biaxial stretching zone.

The shapes and curvatures predicted by the FC and VPSC models are quite different (Fig. 20 left). Within the VPSC framework, the yield loci are sharper, and only small differences can be found between the BCC48 and BCC24 based simulations. This is consistent with the similar limit-strain values predicted by the MK-VPSC model, as shown in Fig. 19. The differences are more pronounced for the MK-FC calculations. The curvature of the BCC24 yield locus is more gradual than that of the BCC48 material, again in agreement with the predicted limit strains. Fig. 20b presents the stress potential in a different but qualitatively similar way, based on the direction of plastic-strain rate and loading direction. In the Cauchy stress reference frame, the directions at different points along the predicted yield surfaces are characterized by two angles, θ and φ, as shown in Fig. 20 (right). These angles are taken to be zero along the horizontal axis and assumed positive in a counterclockwise sense. Differences in the sharpness of the stress potentials in equi-biaxial stretching, reflected in the slope of the plots, are clearly illustrated. For the BCC24-FC case, the direction of the plastic-strain rate $\bar{\mathbf{D}}$, or θ, seems nearly invariant in the vicinity of φ=45º (equi-biaxial strain-rate states), whereas for BCC48-FC the values of θ increase steadily with φ over this range. The curves calculated with the FC theory, in accordance with the observed yield loci, are not steep and clearly different for the two materials. For the BCC48-SC and BCC24-SC materials, the slight changes observed in the predicted critical-strain values correlate to almost identical profiles in Fig. 20b. In the vicinity of φ=45º, the sharpness of both yield loci are characterized by an abrupt change of θ. Over the range $42º \leq \varphi \leq 47º$, θ varies linearly from 23º to 63º. This allows the material to quickly approach a plane-strain state with minor variations of stress state. We verified that this behavior can be mainly attributed to the ability of the VPSC model to distribute the imposed deformation according to the relative hardness of the grains. In addition, we note that a large majority of the grains, approximately 80 percent, shows a similar local-states solution (i.e. stress / strain-rate states, plastic dissipation and accumulated shear), but built from different sets of active slip systems when the simulations were carried out with either BCC48 or BCC24 slip assumptions. Consequently, MK-VPSC predicts very similar limit strains for both microstructural slip assumptions, though this result is specifically dependent on the initial material texture.

In summary, although it is normally accepted that a BCC material can be represented using 24 or 48 slip systems, we found that the MK-FC FLD calculations are sensitive to the material plasticity assumption in the vicinity of equi-biaxial stretching. However, this is not

the case when we follow the MK-VPSC procedure, at least for a nontextured material. For these calculations, we found that either BCC24 or BCC48 materials give similar FLD curves, over the whole range of deformations.

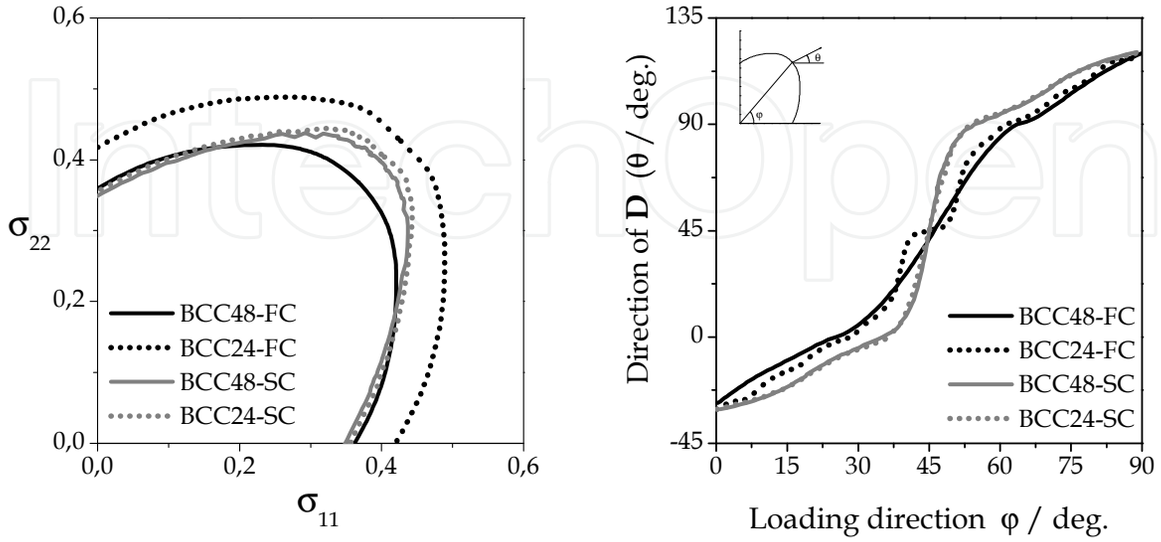


**Figure 20.** Yield loci at equi-biaxial failure for all tested materials (left); directions of the plastic strain-rate vectors (right).

Finally, we evaluated the MK-VPSC capability comparing the predictions of our model with recently published experimental and numerical results. Data and predictions for two low-carbon steel, LCS, sheets are analyzed. The limit-strain calculations performed with MK-FC and MK-VPSC are analyzed and discussed in terms of the crystallographic- slip assumption, and compared with the measured data. All experimental tests were conducted at room temperature.

For a first verification, experimental data are taken from Serenelli et al. (2010). The initial texture of the steel sheet was measured by using a Phillips X'Pert X-ray diffractometer. Incomplete pole figures for the {110}, {200} and {112} diffraction peaks were obtained. From these data, the ODF was determined, and the completed {110} and {100} pole figures were calculated (Fig. 21). The texture was discretized into 1000 orientations of equal volume fraction. Due to the annealing process, the texture contains a slight α-fiber ({001}<110> 1.2%, {112}<110> 9.6%), a more intense γ-fiber ({111}<110> 18.7%, {111}<112> 9.0%), and {554}<225> 11.7%. Optical micrographs of the LCS annealed microstructure show oblate spherical grains, with an approximate aspect ratio of 1.0:1.0:0.4.

Equi-biaxial bulge tests with different elliptical die rings were conducted in order to obtain three biaxial paths in strain space. The die ring masks had a major diameter of 125 mm and aspect ratios of 0.5, 0.7 and 1.0. The die rings and a corresponding tested circle-gridded specimens are shown in Fig. 22. A grid pattern of 2.5 mm diameter circles was electro-chemically etched on the surface of specimens. Details of the experimental procedure can be found in Serenelli et al. (2010).

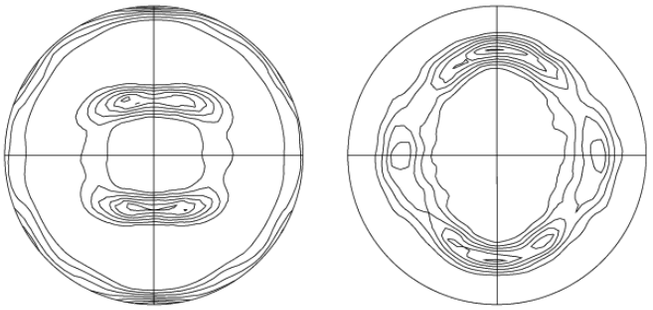


**Figure 21.** Experimental {110} and {100} stereographic pole figures (lines are multiples of a half-random distribution). Reference frame: $X_1$ top (RD), $X_2$ right (TD), $X_3$ center (ND).

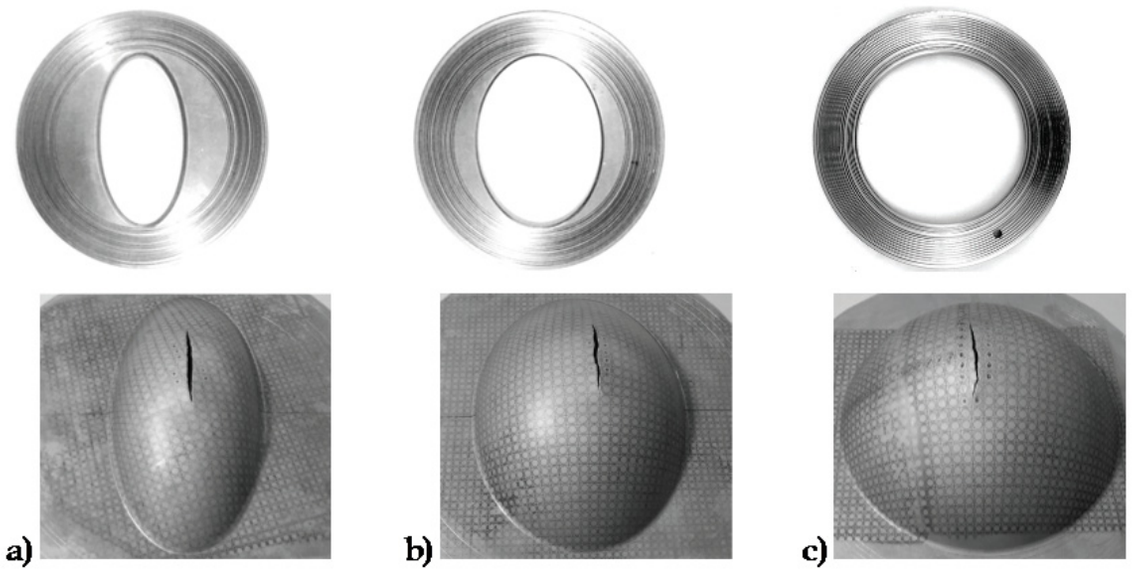


**Figure 22.** Die-ring masks (top) and photograph of the gridded specimens after the tests (bottom) with ratios of 0.5 (a), 0.7 (b) and 1.0 (c) between the major and minor diameters. The marked points where the grid was measured can be observed in the photographs.

The alloy's hardening parameters were estimated in order to fit tensile test data. The coefficients for the BCC48-FC, BCC24-FC, BCC48-SC and BCC24-SC materials are listed in Table 8.

| Material | BCC48-FC | BCC48-SC | BCC24-FC | BCC24-SC |
|---|---|---|---|---|
| $h_0$ (MPa) | 1680 | 2900 | 1770 | 2900 |
| $n$ | 0.203 | 0.212 | 0.201 | 0.212 |
| $\tau_c^s$ (MPa) | 49.0 | 60.0 | 47.5 | 59.0 |

**Table 8.** Material parameters used in the simulations for the LCS sheet.

The initial value of the imperfection factor, $f_0$, was taken to be 0.996. The FLD predictions are shown in Fig. 23 together with the bulge-test data. The BCC48-SC predicted limit-strains agree

well with the measured points. The plane strain behavior is similar to that predicted for an initial non-textured material, and no influence from the crystallographic slip assumption is found. However, the differences between the interaction models remain. In these calculations, the MK-VPSC results showed a sensibility to the addition of {123}<111> slip as a potentially active deformation mode; only BCC48-SC predicts a realistic strain-limit profile.

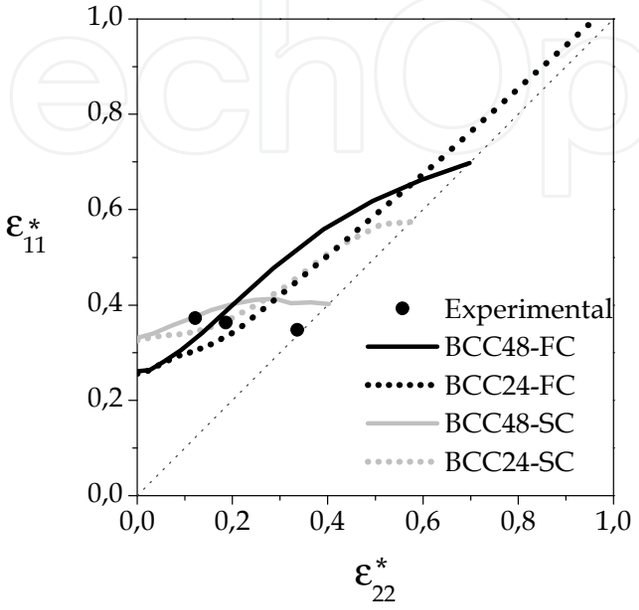


**Figure 23.** Influence of the slip microstructure and interaction model on limit strains for the LCS rolled sheet.

For a second verification, we consider data – experimental FLD and material's properties – from Signorelli et al. (2012) for an electro-galvanized DQ-type steel sheet 0.67 mm thick. Texture measurements were conducted using X-Ray diffraction in a Phillips X'Pert Pro-MPD system equipped with a texture goniometer, Cu*K* alpha radiation and an X-ray lens. The initial pole figures obtained for the {110}, {112} and {100} diffraction peaks are shown in Fig. 24 (left). From these data the ODF was calculated. The measured texture represented by the $\varphi_2$ = 45° section is also presented in Fig. 24 (right). It shows a high concentration of orientations with {111} planes lying parallel to the sample (sheet) surface together with the {554}<225> orientations. This is typical of a cold-rolled and annealed steel.

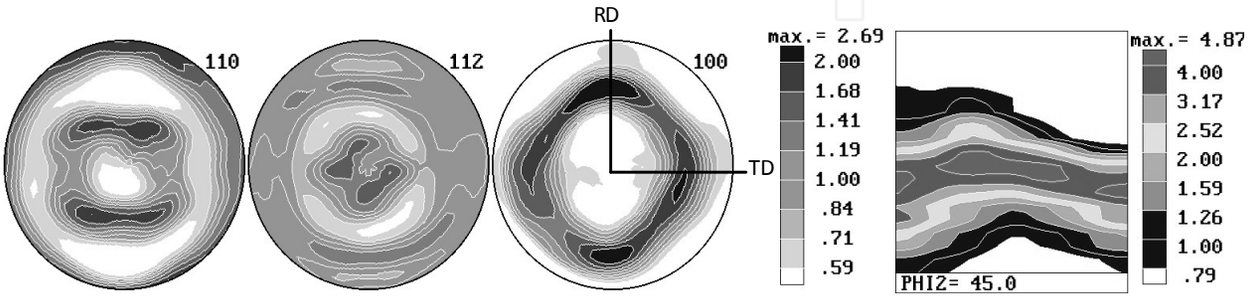


**Figure 24.** Experimental equal-area pole figures {110}, {112} and {100} (left); $\varphi_2$ = 45° section of the ODF (right).

The forming-limit diagrams were determined by following an experimental procedure involving three stages: applying a circle grid to the samples, punch stretching to maximum load, and measuring strains. As we are not focused on the experimental methods and techniques, we will not present experimental details here. Readers are referred to Signorelli et al. (2012) for a completed description of the specific techniques for measuring the FLDs.

Simulations were performed following the methodology described in previous sections. The measured initial texture was discretized into 1000 orientations of equal volume fraction. In this case, we assumed that plastic deformation occurred by slip on the {110}, {112} and {123} planes with a <111> slip direction for each case (BCC48). The hardening parameters were established by numerically fitting the uniaxial tensile data taken parallel to the rolling direction with the following results: $\tau_c^s$ = 62 MPa, $h_0$ = 2275 MPa and $n$ = 0.222 for VPSC simulations; and $\tau_c^s$ = 55 MPa, $h_0$ = 1100 MPa and $n$ = 0.209 for the FC calculations. For the calculations, the initial slip resistances, $\tau_c^s$, of all slip systems are assumed equal, the strain-rate sensitivity and the reference slip rate at the crystal level were taken to be $m$ = 0.02 and $\dot{\gamma}_0^s$ = 1 $s^{-1}$, respectively. The simulated and the experimental curves are shown in Fig. 25.

Before performing simulations, we adjusted $f_0$ such that the predicted limit strains matched the experimental results in plane strain. For the MK-FC and MK-VPSC simulations these values of $f_0$ were 0.999 and 0.996 respectively. Together with the experimental data, the simulated FLDs for both the MK-FC and MK-VPSC schemes are shown in Fig. 26. The open symbols define a safe zone of uniform deformation for metal forming. The solid symbols correspond to measured circles that experienced local necking or fracture, specifying an insecure zone for metal forming.

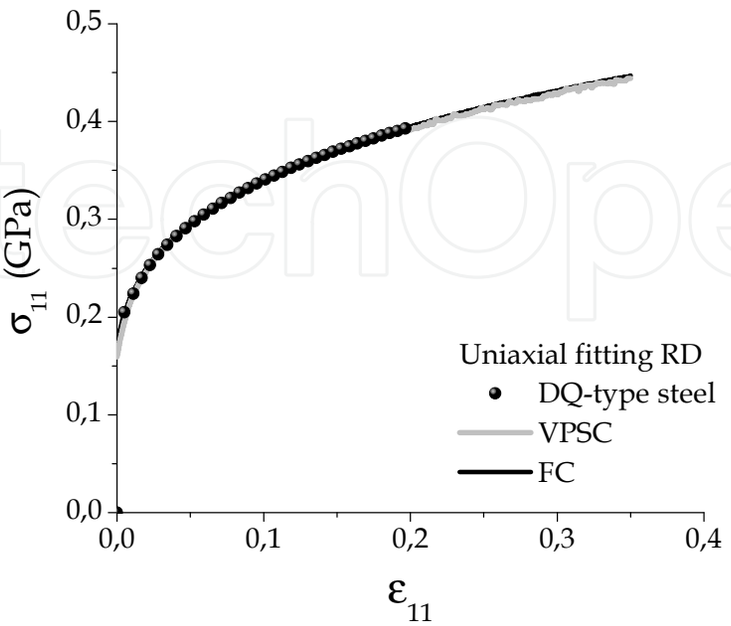


**Figure 25.** Experimental and simulated uniaxial tests parallel to the rolling direction.

The shapes and levels of the predicted FLDs for both models are similar in the tension-compression range, and the trends between measured and simulated limit strains are close, except near uniaxial tension. In this region, simulations show that there are differences between the MK-VPSC and MK-FC schemes. MK-FC predictions are more conservative and this curve lies below the region of localized flow. Examining the calculated FLDs in the biaxial quadrant of strain space, we found that the limit values predicted by MK-VPSC model accurately separate the regions of safe (uniform) and insecure (localized) deformation. On the other hand, the critical values calculated with the MK-FC approach, are only accurate for strain-path values to 0.3. These differences reach a maximum for the equi-biaxial deformation path. Our simulations clearly show that limit values calculated with the MK-FC approach increase unrealistically as ρ increases. It is clear that the VPSC scheme together with the MK approach provides accurate predictions of the DQ-type steel behavior over the entire biaxial range.

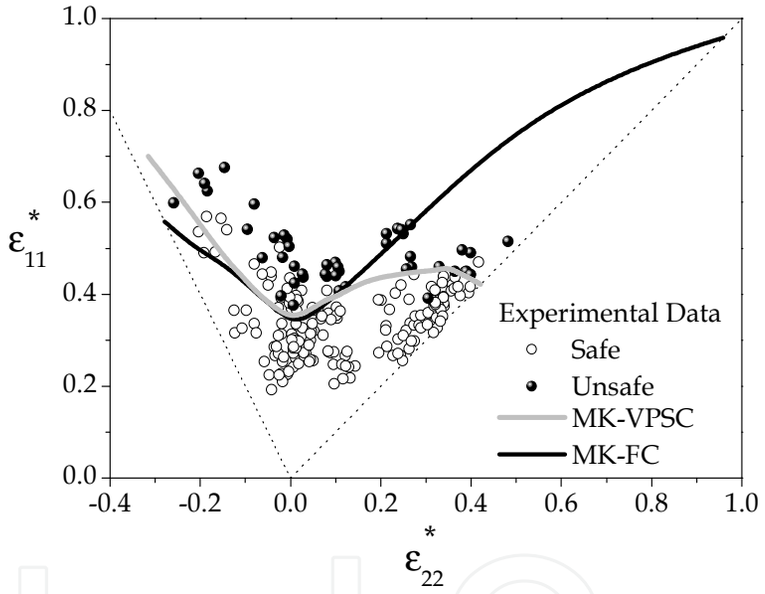


**Figure 26.** Experimental data and simulated FLDs for both MK-FC and MK-VPSC schemes for the DQ-type steel.

## 5.3. Summary

From the results presented in this chapter it can generally be concluded that the calculation of the FLD is strongly influenced by the selected constitutive description. In the present work we highlight the important role that the assumed homogenization scheme plays, which cannot be omitted in the discussion of the simulation's results. The predicative capability of a particular crystal-plasticity model is then assessed by comparing its predictions with those experimental data not used for the fitting. In our case, the discussion is framed in terms of the predicted FLD, texture evolution and polycrystal yield surface.

The emphasis in this chapter has been on cubic metals, and all calculations were carried out using either Full-Contraint or Self-Consistent models. All simulations clearly show that there are differences between the MK-VPSC and MK-FC assumptions, although the shapes and levels of the predicted FLDs are similar in the tension-compression range. Some examples were analyzed in order to highlight these differences:

- Non-textured FCC and BCC materials were investigated, imposing the same uniaxial behaviors for all simulations. The FLDs clearly depended on the homogenization scheme, and those differences were interpreted in terms of the sharpness of the yield-loci and texture development.
- For FCC texture materials, the MK-VPSC approach successfully predicts a smooth transition in the limit strains from the ideal cube texture, through dispersions around the cube texture with increasing cut-off angles, ending with a random texture. Important differences that increase with an increasing spread in texture distribution, particularly near equibiaxial strain-path, were found between the MK-FC and the MK-VPSC models.
- In order to verify the capability of the MK-VPSC model for predicting actual experimental limit strains for BCC textured materials, we carried out simulations for two different LCS steel sheets. The simulations gave good predictions of the steel's behavior over the complete biaxial range. To the contrary, the MK-FC model predicts extremely high limit strains as pure biaxial tension is approached, though both MK-FC and MK-VPSC predictions appear to be accurate on the tensile side of the plane strain.

## Author details

Javier W. Signorelli and María de los Angeles Bertinetti
*Instituto de Física Rosario (IFIR), CONICET–UNR, Rosario, Argentina*

## Acknowledgement

The authors thank M. G. Stout for fruitful comments about the present manuscript.

## 6. References

Asaro, R. & Needleman A. (1985). Texture development and strain hardening in rate dependent polycrystals. *Acta Metallurgica* 33, 923–53.

Barlat, F. (1989). Forming limit diagrams-predictions based on some microstructural aspects of materials. In: *Forming Limit Diagrams: Concepts, Methods and Applications*, Wagoner, R.H., Chan, K.S., Keeler, S.P. (Eds.), 275–302, The Minerals, Metals and Materials Society, Warrendale.

Bunge, H.J. (1982). *Texture Analysis in Materials Science—Mathematical Methods,* (2nd. Ed.), Butterworth, ISBN 0408106425, 9780408106429, London.

Friedman, P.A. & Pan, J. (2000). Effects of plastic anisotropy and yield criteria on prediction of forming limit curves. *International Journal of Mechanical Sciences* 42, 29-48.

Hecker, S.S. (1975). Simple technique for determining FLC. *Sheet Metal Industries* 52, 671-675.

Hiwatashi, S., Van Bael, A., Van Houtte, P. & Teodosiu, C. (1998). Predictions of forming limit strains under strain path changes: applications of an anisotropic model based on texture and dislocation structure. *International Journal of Plasticity* 14, 647-669.

Humphreys, F.J. & Hatherly, M. (2004). *Recrystallization and Related Annealing Phenomena*, (2nd. Ed.), Elsevier Science Ltd., Oxford OX5 IGB, ISBN-10: 008042, UK.

Hutchinson, J.W. (1976). Bound and self-consistent estimated for creep of polycrystalline materials. *Proceedings of the Royal Society of London* A 348, 101-127.

Hutchinson, J.W. & Neale, K.W. (1978). Sheet necking II, time-independent behavior. In: *Mechanics of Sheet Metal Forming*, Koistinen, D.P., Wang, N.M. (Eds.), 127-153, Plenum Press, New York, London,.

Inal, K., Neale, K. & Aboutajeddine, A. (2005). Forming limit comparison for FCC and BCC sheets. *International Journal of Plasticity* 21, 1255-66.

Knockaert, R., Chastel, Y. & Massoni, E. (2002). Forming limits prediction using rate-independent polycrystalline plasticity. *International Journal of Plasticity* 18, 231-47.

Kocks, U.F., Tomé, C.N. & Wenk, H.-R. (1988). *Texture and Anisotropy: Preferred Orientations in Polycrystals and Their Effect on Materials Properties*, Cambridge University Press, ISBN 052179420X, 9780521794206,UK.

Kuroda, M. & Tvergaard,V. (2000). Forming limit diagrams for anisotropic metal sheets with different yield criteria. *International Journal of Solids and Structures* 37, 5037-59.

Lebensohn, R.A. & Tomé C.N. (1993). A self-consistent approach for the simulation of plastic deformation and texture development of polycrystals: application to Zr alloys. *Acta Metallurgica et Materialia* 41, 2611-2624.

Lee, W.B. & Wen, X.Y. (2006). A dislocation-model of forming limit prediction in the biaxial stretching of sheet metals. *International Journal of the Mechanical Sciences* 48, 134-44.

Lian, J., Barlat, F. & Baudelet, B. (1989). Plastic behavior and stretchability of sheet metals. II. Effect of yield surface shape on sheet forming limit. *International Journal of Plasticity* 5, 131-147.

Marciniak, Z. & Kuczynski, K. (1967). Limit strains in the process of stretch-forming sheet metal. *International Journal of the Mechanical Sciences* 9, 609–20.

Mura, T. (1987). *Micromechanics of Defects in Solids*. Martinus Nijhoff Publishers, Dordrecht, ISBN 9024732565, 9789024732562, The Netherlands.

Neale, K.W. & Chater, E. (1980). Limit strain predictions for strain-rate sensitive anisotropic sheets, *International Journal of the Mechanical Sciences* 22, 563-574.

Neil, J.C. & Agnew, S.R. (2009). Crystal plasticity-based forming limit prediction for non-cubic metals: Application to Mg alloy AZ31B. *International Journal of Plasticity* 25 (3), 379-98.

Ray, R.K., Jonas, J.J. & Hook, R. E. (1994). Cold rolling and annealing textures in low carbon and extra low carbon steels, *International Materials Reviews* 39 (4), 129-172.

Roters, F., Eisenlohr, P., Bieler, T. & Raabe, D. (2010). Introduction to Crystalline Anisotropy and the Crystal Plasticity Finite Element Method, In: *Materials Science and Engineering*, Wiley-Vch Verlag GmbH & Co. KGaA, ISBN: 978-3-527-32447-7, Weinheim.

Serenelli, M.J., Bertinetti, M.A. & Signorelli, J.W. (2010). Investigation of the Dislocation Slip Assumption on Formability of BCC Sheet Metals. *International Journal of the Mechanical Sciences* 52, 1723-1734.

Serenelli, M.J., Bertinetti, M.A. & Signorelli, J.W. (2011). Study of limit strains for FCC and BCC sheet metal using polycrystal plasticity. *International Journal of Solids and Structures* 48, 1109-1119.

Signorelli, J.W., Bertinetti, M.A. & Turner, P.A. (2009). Predictions of forming limit diagrams using a rate-dependent polycrystal self-consistent plasticity model. *International Journal of Plasticity* 25 (1), 1-25.

Signorelli, J.W. & Bertinetti, M.A. (2009). On the Role of Constitutive Model in the Forming Limit of FCC Sheet Metal with Cube Orientations. *International Journal of the Mechanical Sciences* 51 (6), 473-480.

Signorelli, J.W., Bertinetti, M.A. & Serenelli, M.J. (2012). Experimental and numerical study of the role of crystallographic texture on the formability of an electro-galvanized steel sheet. *Journal of Materials Processing Technology* 212, 1367-1376.

Storen, S. & Rice, J.R. (1975). Localized necking in thin sheet. *Journal of the Mechanics and Physics of Solids* 23, 421–41.

Tang, C.Y. & Tai, W.H. (2000). Material damage and forming limits of textured sheet metals. *Journal of Materials Processing Technology* 99, 135-140.

Tóth, L., Dudzinski, D. & Molinari, A. (1996). Forming limit predictions with the perturbation method using stress potential functions of polycrystal visco- plasticity. *International Journal of the Mechanical Sciences* 38, 805-24.

Wu P.D., Neale K.W. & Giessen V.D. (1997). On crystal plasticity FLD analysis. *Proceedings of the Royal Society of London* A 453, 1831-48.

Wu, P.D., MacEwen, S.R., Lloyd, D.J. & Neale, K.W. (2004a). Effect of cube texture on sheet metal formability. *Materials Science and Engineering* A 364, 182-7.

Wu, P.D., MacEwen, S.R., Lloyd, D.J. & Neale, K.W. (2004b). A mesoscopic approach for predicting sheet metal formability. *Modelling and Simulation in Materials Science and Engineering 12*, 511-527.

Wu, P.D., Graf, A., Mac Ewen, S.R., Lloyd, D.J., Jain, M. & Neale, K.W., 2005. On forming limit stress diagram analysis. *International Journal of Solids and Structures* 42, 2225-2241.

Yoshida, K., Ishizaka, T., Kuroda, M. & Ikawa, S. (2007). The effects of texture on formability of aluminum alloys sheets. *Acta Materialia* 55, 4499-506.

Zhou, Y. & Neale, K.W. (1995). Predictions of forming limit diagrams using a rate-sensitive crystal plasticity model. *International Journal of the Mechanical Sciences* 37, 1-20.